Cortical control of virtual self-motion using task-specific subspaces

Karen E Schroeder* [1,2], Sean M Perkins* [2,3], Qi Wang[3], & Mark M Churchland[1,2,4,5, †]

* Equal contribution

[1] Department of Neuroscience, Columbia University Medical Center, New York, NY
[2] Zuckerman Institute, Columbia University, New York, NY
[3] Department of Biomedical Engineering, Columbia University, New York, NY
[4] Kavli Institute for Brain Science, Columbia University Medical Center, New York, NY
[5] Grossman Center for the Statistics of Mind, Columbia University, New York, NY

[†] Correspondence to: mc3502@columbia.edu

1 Abstract

2 Brain-machine interfaces (BMIs) for reaching have enjoyed continued performance

3 improvements, yet there remains significant need for BMIs that control other movement

4 classes. The question of how to decode neural activity is inexorably linked with the intrinsic

5 covariance structure of that activity, which may depend strongly upon movement class. Here,

6 we develop a self-motion BMI based on cortical activity as monkeys cycle a hand-held pedal

7 to progress along a virtual track. Unlike during reaching, there were no high-variance

8 dimensions that directly correlated with to-be-decoded variables. Yet this challenge yielded an

9 opportunity: we could decode a single variable – self-motion – by non-linearly leveraging

10 structure that spanned many high-variance neural dimensions. Online BMI-control success

11 rates approached those during manual control. Our results argue that decoding can and

12 should be task-specific, and suggest a broad principle: even when the decoded output is low-

13 dimensional, it can be beneficial to leverage a multi-dimensional high-variance subspace.

Introduction

14

15   Intracortical brain-machine interfaces (BMIs) that support reach-like tasks have proved

16   successful in primates and human clinical trials (Ajiboye et al., 2017; Collinger et al., 2013;

17   Ethier et al., 2012; Gilja et al., 2015, 2012; Shanechi et al., 2017; Shenoy and Carmena, 2014;

18   Wodlinger et al., 2015). Yet it is unclear whether current decode algorithms will generalize well

19   to non-reaching applications. Early reach-based BMIs (Carmena et al., 2003; Chapin et al.,

20   1999; Serruya et al., 2002; Taylor et al., 2002; Velliste et al., 2008; Wessberg et al., 2000)

21   employed a strategy of inverting the ostensible neural encoding of kinematic variables,

22   primarily hand velocity and direction. Despite evidence against literal kinematic encoding

23   (Churchland et al., 2012; Michaels et al., 2016; Russo et al., 2018; Scott et al., 2001; Sergio et

24   al., 2005; Sussillo et al., 2015), studies continue to exploit the robust correlation between

25   neural activity and movement direction to achieve excellent BMI performance. Improvements

26   have derived from honing this core strategy and/or better estimating the neural state

27   (Aghagolzadeh and Truccolo, 2016; Gilja et al., 2012; Kao et al., 2015; Makin et al., 2018).

28   Viewed this way, current decode strategies successfully leverage a statistical regularity

29   (aspects of neural activity correlate with velocity) that is sizeable during reach-like movements.

30   Should non-reach-like movements leverage the same or different statistical regularities?

31   This question is intertwined with our evolving understanding of motor cortex covariance

32   structure. During a given task, neural covariance is typically low-dimensional, in the sense that

33   a handful of neural dimensions captures considerable variance (Churchland et al., 2007;

34   Gallego et al., 2017; Sadtler et al., 2014). Nevertheless, dimensions with non-negligible

35   variance greatly outnumber to-be-decoded variables (Churchland and Shenoy, 2007; Shenoy

36   et al., 2013). The traditional solution is to identify a subspace where population activity is both

37   reasonably high-variance and correlates strongly with variables one wishes to infer. For

38   example, regressing two-dimensional cursor velocity against neural activity identifies a two-

39   dimensional neural subspace where activity resembles velocity. A few studies have

40   successfully leveraged additional dimensions (Degenhart et al., 2020; Gallego et al., 2020; Kao

41   et al., 2017b; Sussillo et al., 2016, 2012), but the typical scenario is that decoding N variables

42   leverages an N-dimensional subspace chosen to maximize correlations.

43   Within a given task, neural covariance structure remains surprisingly fixed even when the

44   decoder is altered (Golub et al., 2018; Sadtler et al., 2014) and can remain similar across

45   related tasks (Gallego et al., 2018). Yet covariance is often not stable. Covariance changes

46   dramatically when cycling forward versus backward (Russo et al., 2018), when using one arm

47   versus another (Ames and Churchland, 2019), when preparing versus moving (Elsayed et al.,

48   2016; Kaufman et al., 2014), and when reaching versus walking (Miri et al., 2017). Thus, there

49   may be no high-variance task-independent subspace that consistently exhibits correlations

50   with to-be-decoded variables. This would agree with the view that the highest-variance signals

51   in motor cortex ensure noise-robust task-specific dynamics and do not reliably encode any

52   external quantity (Russo et al., 2018). This possibility creates challenges, but also

53   opportunities. Task-specific subspaces may be of high utility even when there is no linear

54   correlation between activity and a decoded variable. For example, one could decode forward

55   self-motion from the angular momentum of neural activity in a two-dimensional subspace. To

56   guide backward self-motion, a completely different neural subspace could be employed. Thus,

57   a one-dimensional output could potentially leverage activity spanning many dimensions.

58   To explore such strategies, we employed a simple task in which monkeys cycle a hand-held

59   pedal to move along a virtual track. The class of neural activity evoked by this task could

60   potentially be leveraged by future BMI devices that guide self-motion. Even more critically,

61   cycling is overtly different from reach- or joystick-based tasks. Prior explorations of self-

62   motion-decoding borrowed from the strategies employed by reach-based BMIs, and decoded

63   a whole-body directional vector (Rajangam et al., 2016) or classified the direction of a joystick

64   intermediary (Libedinsky et al., 2016). This is a promising approach, but we wished to explore

65   whether a task-specific approach might also be promising.

66   During cycling, neural activity that correlated with kinematics and/or muscle activity was

67   relegated to low-variance subspaces. In contrast, there existed high-variance subspaces

68   where neural activity had reliable non-linear relationships with intended self-motion. A decoder

69   leveraging those multi-dimensional subspaces provided excellent online control of a one-

70   dimensional command for virtual self-motion. Almost no training was needed; decoder latency

71   and accuracy were such that monkeys appeared to barely notice transitions from manual

72   control to BMI control. Success rates and acquisition times were close to those achieved

73   under manual control. Our results establish that BMIs can be accurately guided by strategies

74   that leverage task-specific subspaces containing structure that, while not directly correlating

75   with kinematic variables, bears a reliable relationship with desired movement.

76

4

Results

Behavior

We trained two monkeys (G and E) to rotate a hand-held pedal to move through a virtual environment (**Fig. 1**). All motion was along a linear track – no steering was necessary. Consistent with this, a single pedal was cycled with the right arm only. Our goal when decoding was to reconstruct the virtual self-motion produced by that single pedal. On each trial, a target appeared in the distance. To acquire that target, monkeys produced virtual velocity in proportion to the rotational velocity of the pedal. The color of the environment (lush and green versus desert-like and tan) instructed cycling direction. When the environment was green (**Fig. 1a**, *left*) forward virtual motion was produced by cycling 'forward' (i.e., with the hand moving away from the body at the top of the cycle). When the environment was tan (**Fig. 1a**, *right*) forward virtual motion was produced by cycling 'backward' (the hand moving toward the body at the top of the cycle). Cycling in the wrong direction produced motion away from the target. Trials were presented in blocks of forward or backward trials. Within each block, targets were separated by a randomized distance of 2, 4 or 7 cycles. Acquisition of a target was achieved by stopping and remaining stationary 'on top' of the virtual target for a specified time. Reward was then given and the next target appeared.

Monkeys performed the task well, moving swiftly between targets, stopping accurately on each target, and remaining stationary until the next target was shown. Monkeys cycled at a pace that yielded nearly linear progress through the virtual environment (**Fig. 1b**). Although not instructed to cycle at any particular angular velocity, monkeys adopted a brisk ~2 Hz rhythm (**Fig. 1c**). Small ripples in angular velocity were present during steady-state cycling; when cycling with one hand it is natural for velocity to increase on the downstroke and decrease on the upstroke. Success rates were high, exceeding 95% in every session (failures typically involved over- or under-shooting the target location). This excellent performance under manual control provides a stringent bar by which to judge performance under BMI control.

BMI control was introduced after monkeys were adept at performing the task under manual control. Task structure and the parameters for success were unchanged under BMI control, and no cue was given regarding the change from manual to BMI control. The switch to BMI control was made after completion of a block of manual-control trials (25 forward and 25 backward 7-cycle trials). These manual-control trials were used to train the decoder, at which
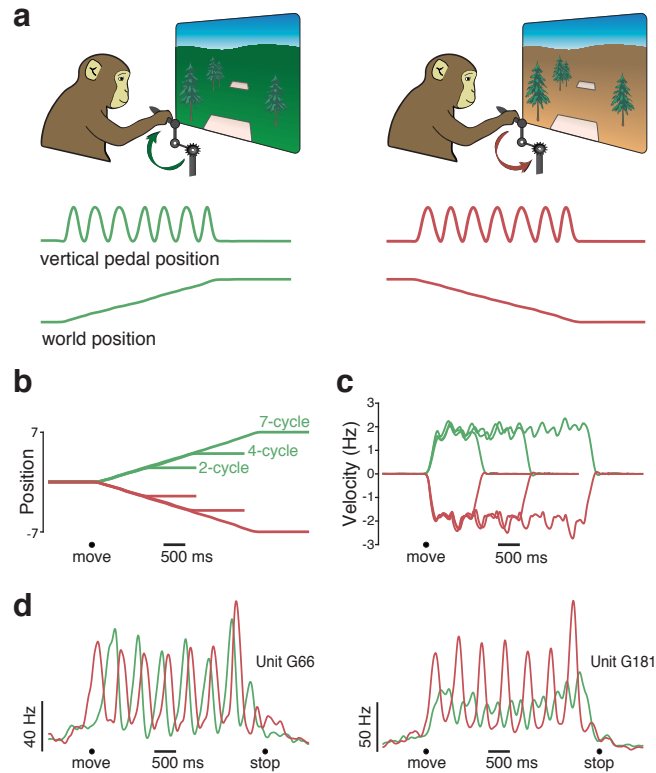
5

Figure 1. A cycling task that elicits rhythmic movements. (a) Monkeys rotated a hand-held pedal forward (*left*, cued by a green background) or backward (*right*, cued by a tan background) to progress through a virtual environment. Traces at bottom plot pedal kinematics (vertical position) and the resulting virtual world position for two example manual-control trials. On both of these trials (one forward and one backward) the monkey progressed from one target to another by cycling seven cycles. **(b)** Trial-averaged virtual position from a typical manual-control session. Each trace plots the change in virtual position (from a starting position of zero) for one of six conditions: forward or backward for 2, 4, or 7 cycles. Black circle indicates the time of movement onset. Trials were averaged after being aligned to movement onset, and then scaled such that the duration of each trial matched the average duration for that condition. **(c)** Trial-averaged pedal rotational velocity from the same session, for the same six conditions. **(d)** Firing rates of two example units. Trial-averaged firing rates (computed after temporally aligning trials) are shown for two conditions: forward (*green*) and backward (*red*) for seven cycles. Black circles indicate the timing of movement onset and offset.

108   point the switch was made to BMI control for the remainder of the session. For monkey G, we

109   occasionally included blocks of manual-control trials later in the session to allow comparison

110   between BMI and manual performance. For Monkey E we used separate (interleaved) sessions

111   to assess manual-control performance.

112   During both BMI control and manual control, the monkey's ipsilateral (non-cycling) arm was

113   restrained. The contralateral (cycling) arm was never restrained. We intentionally did not

114   dissuade the monkey from continuing to physically cycle during BMI control. Indeed, our goal

115   was that the transition to BMI control would be sufficiently seamless to be unnoticed by the

116   monkey, such that he would still believe that he was in manual control. An advantage of this

117   strategy is that we are decoding neural activity when the subject attempts to actually move, as

118   a patient presumably would. Had we insisted the arm remain stationary, monkeys would have

119   needed to actively avoid patterns of neural activity that drive movement – something a patient

120   would not have to do. Allowing the monkey to continue to move normally also allowed us to

121   quantify decoder performance via direct comparisons with intended (i.e., actual) movement.

122   This is often not possible when using other designs. For example, in Rajangam et. al.

123   (Rajangam et al., 2016), performance could only be assessed via indirect measures (e.g., time

124   to target) because what the monkey was actually intending to do at each moment was unclear.

125   We considered these advantages to outweigh a potential concern: a decoder could potentially

126   'cheat' by primarily leveraging activity driven by proprioceptive feedback (which would not be

127   present in a paralyzed patient). This is unlikely to be a large concern. Recordings were made

128   from motor cortex, where robust neural responses precede movement onset. Furthermore, we

129   have documented that motor cortex population activity during cycling is quite different from

130   that within the proprioceptive region of primary somatosensory cortex (Russo et al., 2018).

131   Thus, while proprioceptive activity is certainly present in motor cortex (Fetz et al., 1980; Lemon

132   et al., 1976; Schroeder et al., 2017; Suminski et al., 2009) especially during perturbations

133   (Pruszynski et al., 2011), the dominant features of M1 activity that we leverage are unlikely to

134   be primarily proprioceptive.

135   Given our use of healthy animals, we stress that the goal of the present study is to determine

136   strategies for leveraging the dominant structure of neural activity. This follows the successful

137   strategy of BMI studies that leveraged the well-characterized structure of activity during

138   reaching. Of course, the nature of the training data used to specify decode parameters (e.g.,

139   the weights that define the neural dimensions to be used) will necessarily be different for a

6

140 healthy animal that cannot understand verbal instructions and an impaired human that can. We

141 thus stress that our goal is to determine a robust and successful decode strategy that works in

142 real time during closed-loop performance. We do not attempt to determine the best approach

143 to parameter specification, which in a patient would necessarily involve intended or imagined

144 movement.

145 ***Neural activity and decoding strategy***

146 We recorded motor cortical activity using 96-channel Utah arrays. For monkey G, one array

147 was implanted in primary motor cortex (M1) and a second in dorsal premotor cortex (PMd). For

148 monkey E, a single array was implanted in M1. For each channel we recorded times when the

149 voltage crossed a threshold. Threshold crossings typically reflected individual spikes from a

150 small handful of neurons (a neural 'unit'). Spikes from individual neurons could be clearly seen

151 on many channels, but no attempt was made to spike-sort. The benefit of sorting is typically

152 modest when controlling a prosthetic device (Christie et al., 2014), and reduced-dimension

153 projections of motor cortex population activity are similar whether based on single or multi-

154 units (Trautmann et al., 2019). Unit activity was strongly modulated during cycling (**Fig. 1d**). The

155 phase, magnitude, and temporal pattern of activity depended on whether cycling was stopped,

156 moving forward (*green* traces) or moving backward (*red* traces). A key question is how these

157 unit-level features translate into population-level features that might be leveraged to estimate

158 intended motion through the virtual environment.

159 In traditional decoding approaches (**Fig. 2a**) neural activity is hypothesized (usefully if not

160 literally) to encode kinematic signals, which can be decoded by inverting the encoding scheme.

161 Although nonlinear methods (including variations of Kalman filtering) are often used to estimate

162 the neural state, the final conversion to a kinematic command is typically linear or roughly so.

163 To explore kinematic encoding in the present task, we used linear regression to identify neural

164 dimensions where activity correlated well with kinematics (including hand velocity and

165 position). Regression was performed using single trials. Use of single trials provides a large

166 quantity of training data and is implicitly regularizing: regression must find signals that are

167 robust in the face of single-trial spiking variability. The regression weights for a given kinematic

168 parameter define a neural dimension where activity correlates strongly with that parameter. We

169 computed the neural variance captured by each such dimension. Variance captured was

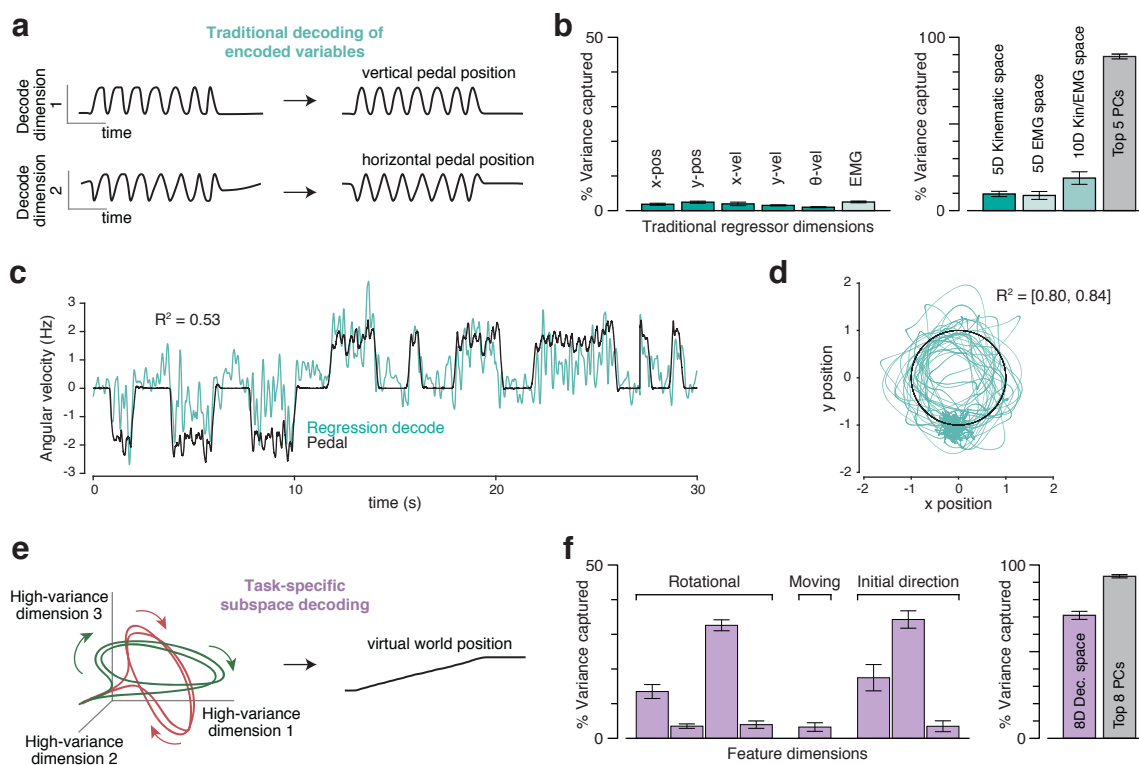170 computed using trial-averaged data, to ensure that values were not diluted by noise. Despite

7

Figure 2. Different decode strategies leverage neural signals with different magnitudes.
(a) In the traditional decoding strategy, neural firing rates are assumed to predominantly encode the key variables. The encoding model is usually assumed to be roughly linear when variables are expressed appropriately. For example, cosine tuning for reach velocity is equivalent to a linear dependence on horizontal and vertical velocity. The goal of decoding is to invert encoding. Thus, decoding dimensions should capture the dominant signals in the neural data (because those are what is encoded). **(b)** Variance of the neural population response captured by dimensions used to decode kinematic parameters (*teal bars*) and muscle activity (*light teal bar*). Data are from three manual-control sessions where units (192 channels per day) and muscles (5-7 channels per day) were recorded simultaneously. Each bar plots the average and standard error across sessions (unless otherwise specified). *Left subpanel*: variance captured for kinematic variables (individual variables shown separately) and muscles (average across 19 recordings, standard error computed across recordings). *Right subpanel*: total variance captured by subspaces spanned by kinematic-decoding dimensions, muscle-decoding dimensions, or both. (These are not the sum of the individual variances as dimensions were not always orthogonal). We had different numbers of EMG recordings per day and thus always selected a subset of five. Variance captured by the top five principal components is shown for comparison. **(c)** Example cross-validated regression performance for offline decoding of angular velocity. R^2 is the coefficient of determination for the segment of data shown. **(d)** Example cross-validated regression performance for offline decoding of horizontal and vertical pedal position. R^2 is the coefficient of determination for the segment of data shown, same time period as (c). **(e)** A new strategy that can be applied even if the dominant signals do not have the goal of encoding. This strategy seeks to find neural response features that have a robust relationship with the variable one wishes to decode. That relationship may be complex or even incidental, but is useful if it involves high-variance response features. **(f)** Similar plot to (b) but for the dimensions upon which our decoder was built. *Left subpanel*: variance captured for each of these eight dimensions. *Right subpanel*: variance captured by the eight-dimensional subspace spanned by those dimensions. Variance captured by the top eight principal components is shown for comparison.

171   this, the neural dimensions that best captured kinematic signals captured little population

172   response variance (**Fig. 2b**, *teal* bars). This was also true of neural dimensions that captured

173   muscle activity (**Fig. 2b**, *light teal* bar). This was initially surprising: single-neuron responses

174   were robustly sinusoidally modulated, as were many kinematic variables. Yet sinusoidal

175   response features were often superimposed upon other response features (e.g., overall shifts in

176   rate when moving versus not moving). Sinusoidal features also did not display phase

177   relationships, across forward and backward cycling, consistent with kinematic encoding

178   (Russo et al., 2018). As a result, the dimensions where activity correlated strongly with

179   kinematics captured relatively little response variance.

180   The fact that kinematic-encoding neural dimensions are low-variance makes them a potentially

181   challenging basis for decoding. For example, we identified a dimension where the projection of

182   trial-averaged neural activity correlated with angular velocity, which is conveniently proportional

183   to the quantity we wish to decode (velocity of virtual self-motion). However, because that

184   dimension captured relatively little variance (1.0% ± 0.2% of the overall population variance;

185   standard deviation across three sessions) the relevant signal was variable on single trials (**Fig.**

186   **2c**) and the correlation with angular velocity was poor ($R^2 = 0.52 ± 0.14$). Any decode based on

187   this signal would result in many false starts and false stops. The observed single-trial variability

188   is expected for any low-variance signal estimated from a limited number of neurons.

189   We considered an alternative kinematic decoding strategy that more closely mimics prior

190   successful reach-based approaches: decoding horizontal and vertical hand position. These

191   were captured in slightly higher-variance dimensions, and could be decoded somewhat better

192   on single trials ($R^2 = [0.81 ± 0.03, 0.85 ± .04]$, averaged across three sessions). A reasonable

193   strategy would be to convert this two-dimensional neural signal (**Fig. 2d**) into a one-dimensional

194   self-motion command. Possible approaches for doing so include deciphering where on the circle

195   the hand is most likely to be at each moment, computing the angular velocity of the neural state,

196   or computing its angular momentum. However, consideration of such approaches raises a

197   deeper question. If we are willing to non-linearly decode a one-dimensional quantity (self-

198   motion) from a two-dimensional subspace, why stop at two dimensions? Furthermore, why not

199   leverage dimensions that capture most of the variance in the population response, rather than

200   dimensions that capture a small minority? Projections onto high-variance dimensions have

201   proportionally less contribution from spiking variability. They are also less likely to be impacted

202   by electrical interference or recording instabilities. While of little concern in a controlled

203   laboratory environment, this is relevant to the clinical goals of prosthetic devices. One should

204   thus wish to leverage multiple dimensions that jointly capture as much variance as possible, so

205   long as the signals captured by those dimensions can be successfully leveraged.

206   We term this approach (**Fig. 2e**) task-specific subspace decoding, because it seeks one or more

207   subspaces that capture robust response features as the subject attempts to move within the

208   context of a particular task (in the present case, while generating a rhythmic movement to

209   produce self-motion). Both the population-level response features, and the subspaces

210   themselves, may be specific to that task. To pursue this strategy, we identified three high-

211   variance subspaces. The first was spanned by four 'rotational dimensions' (two each for

212   forward and backward cycling) which captured elliptical trajectories present during steady-

213   state cycling (Russo et al., 2018). The second was a single 'moving-sensitive' dimension, in

214   which the neural state distinguished whether the monkey was stopped or moving regardless of

215   movement direction (Kaufman et al., 2016). The third was a triplet of 'initial-direction'

216   dimensions, in which cycling direction could be transiently distinguished in the moments after

217   cycling began.

218   In subsequent sections we document the specific features present in these high-variance

219   subspaces. Here we concentrate on the finding that the eight-dimensional space spanned by

220   these eight dimensions captured 70.9% ± 2.3% of the firing-rate variance (**Fig. 2f**). Note that

221   because dimensions are not orthogonal, the total captured variance is not the sum of that for

222   each dimension. The 'initial direction' dimensions, for example, overlap considerably with the

223   'rotational dimensions.' Nevertheless, the total captured variance was only modestly less than

224   that captured by the top eight PCs (which capture the most variance possible), and much

225   greater than that captured by spaces spanned by dimensions where activity correlated with

226   kinematics and/or muscle activity (**Fig. 2b**). We thus based our BMI decode on activity in these

227   eight high-variance dimensions.

Direction of steady-state movement inferred from rotational structure

229   The dominant feature of the population neural response during steady-state cycling was a

230   repeating elliptical trajectory (Russo et al., 2018). Thus, the core of our decoder was built upon

231   this feature, leveraging the fact that forward-cycling and backward-cycling trajectories

232   occurred in non-identical subspaces (**Fig. 3a,b**). We employed an optimization procedure to

233   find a two-dimensional 'forward plane' that maximized the size of the forward trajectory relative
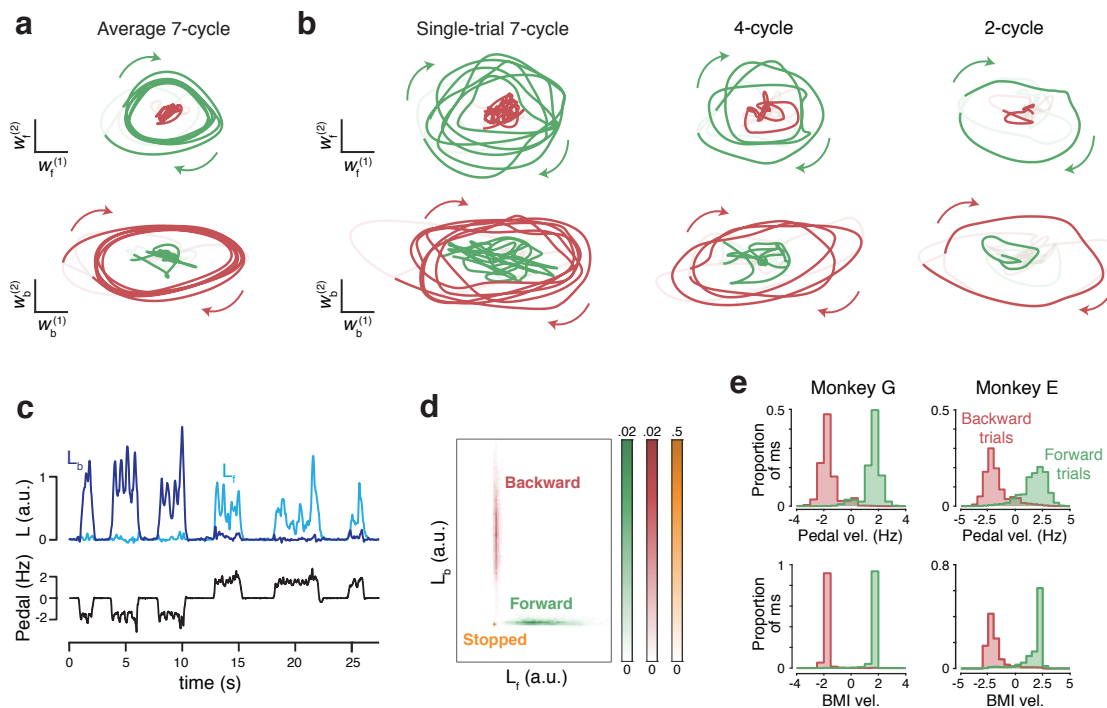
9

Figure 3. Leveraging rotational trajectories to decode velocity. (a) Trial-averaged population activity, during a manual-control block, projected onto the forward (*top*) and backward (*bottom*) rotational planes. Data are from seven-cycle forward (*green*) and backward (*red*) conditions. By design, the forward plane primarily captures rotational trajectories during forward cycling, and vice versa. Boldly colored portions of each trace highlight rotations during the middle cycles (a period that excludes the first and last half cycle of each movement). Colored arrows indicate rotation direction. Light portion of each trace corresponds to the rest of the trial. In addition to smoothing with a causal filter, neural data have been high-pass filtered to match what was used during BMI control. Data are from monkey G. **(b)** As in panel (a), but for three example single trials, one for each of the three distances. **(c)** Example angular momentum (L) in the backward plane (*dark blue*) and forward plane (*bright blue*) during six trials of BMI control. Velocity of the pedal is shown in black. Although the pedal was disconnected, this provides a useful indication of how the monkey was intending to move. Data are from the same day shown in panels **a** and **b**. **(d)** Probability densities of angular momentums found from the training dataset collected on the same day. **(e)** Histograms of BMI-control velocity (*bottom*) and (disconnected) pedal velocity (*top*) for all times the decoder was in the STEADY state (see Methods), across all BMI-control sessions.

234   to the backward trajectory. We similarly found an analogous 'backward plane'. These planes

235   were identified based on trial-averaged responses from the 50 trials of training data collected

236   under manual control (**Fig. 3a**). With the aid of filtering (*Methods*), these planes continued to

237   capture rotational features on individual trials (**Fig. 3b**). Although forward and backward

238   trajectories were not orthogonal to one another, the above procedure was still able to find

239   planes where strongly elliptical trajectories were present for only one cycling direction. To

240   convert the four-dimensional neural state to a one-dimensional decode of self-motion, we

241   compared angular momentum (the cross product of the state vector with its derivative)

242   between the two planes. When moving backward (first three cycling bouts in **Fig. 3c**) angular

243   momentum was sizeable in the backward plane (*dark blue*) but not the forward plane (*bright*

244   *blue*). The opposite was true when moving forward (subsequent three bouts).

245   Based on training data, we considered the joint distribution of forward-plane and backward-

246   plane angular momentum. We computed distributions when stopped (**Fig. 3d**, *orange*), when

247   cycling forward (*green*) and when cycling backward (*red*). These distributions overlapped little,

248   and we fit a Gaussian to each. During BMI control, we computed the likelihood of the observed

249   angular momentums under each of the three distributions. If likelihood under the stopped

250   distribution was high, decoded velocity was zero. Otherwise, decoded velocity was determined

251   by the relative likelihoods under the forward and backward distributions. These likelihoods

252   were converted into a virtual velocity that was maximal when one likelihood was much higher

253   and slower when likelihoods were more similar. The maximum decoded virtual velocity was set

254   to approximate the typical virtual velocity under manual control, when cycling at ~2 Hz.

255   Distributions of decoded velocity when moving under BMI control (**Fig. 3e**, *bottom*) were

256   similar to the distributions of velocity that would have resulted were the pedal still operative

257   (**Fig. 3e**, *top*). Importantly, distributions overlapped very little; the direction of decoded motion

258   was almost always correct. Decoded velocity was near maximal at most times, especially for

259   monkey G. The decoded velocity obtained from these four dimensions (out of the eight total we

260   used) constituted the core of our decoder. We document the performance of that decoder in

261   the next section. Later sections describe how aspects of the decoder were fine-tuned by

262   leveraging the remaining four dimensions.

10

Performance

Monkeys performed the task very well under closed-loop BMI control (**Fig. 4** and **Supp. Movie 1**). Monkeys continued to cycle as normal, presumably not realizing that the pedal had been disconnected from the control system. The illusion that the pedal still controlled the task was supported by a high similarity between decoded virtual velocity and intended virtual velocity (i.e., what would have been produced by the pedal were it still controlling the task). The cross-correlation between these peaked at 0.93 ± .02 and 0.81 ± .03 (monkey G and E, mean ± SD across sessions) at a short lag: 76 ± 4 ms and 102 ± 7 ms (**Fig. 4a**). That illusion was also aided by a low rate of false starts; it was exceedingly rare for decoded motion to be non-zero when the monkey was attempting to remain stationary on top of a target. False starts occurred on 0.29% and 0.09% of trials (monkeys G and E), yielding an average of 1.9 and 0.12 occurrences per day. This is notable because combatting unintended movement is a key challenge for BMI decoding. The above features – high correlation with intended movement, low latency, and few false starts – led to near-normal performance under BMI control (**Fig. 4b,c**). Success rates under BMI control (**Fig. 4d**, *magenta symbols*) were almost as high as under manual control (*open symbols*), and the time to move from target to target was only slightly greater under BMI control (**Fig. 4e**).

The only respect in which BMI control suffered noticeably was accuracy in stopping on the middle of the target. Under manual control, monkeys stopped very close to the target center (**Fig. 4f,** *gray histogram*), which always corresponded to the 'pedal-straight-down' position. Stopping was less accurate under BMI control (*magenta histogram*). This was partly due to the fact that because virtual self-motion was swift, small errors in decoded stopping time became relevant. E.g., a 100 ms error corresponded to ~0.2 cycles of physical motion. The average standard deviation of decoded stopping time (relative to actual stopping time) was 133 (monkey G) and 99 ms (monkey E). The relatively larger error in BMI-control trials was also due to an incidental advantage of manual control: the target center was aligned with the pedal-straight-down position, a fact which monkeys leveraged to stop very accurately in that position. This strategy was not available during BMI control because the correct moment to stop rarely aligned perfectly with the pedal-straight-down position (this occurred only if decoded and intended virtual velocity matched perfectly when averaged across the cycling bout).

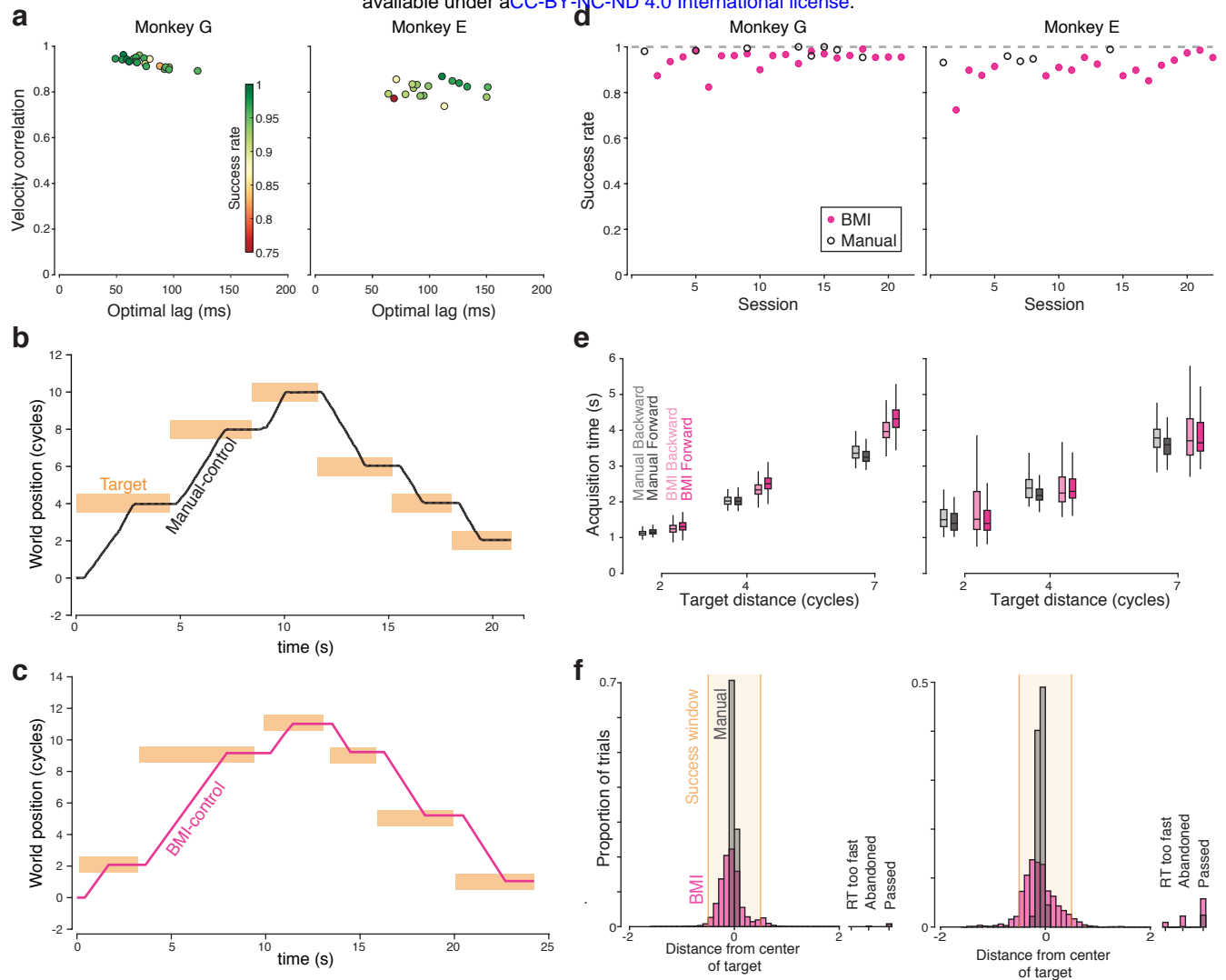**Figure 4. Decoder performance. (a)** Summary of the cross-correlation between decoded virtual velocity under BMI control, and the virtual velocity that would have been produced by the pedal (which monkeys continued to manipulate normally). Each symbol corresponds to one BMI-control session, and plots the peak of the cross-correlation versus the lag where that peak occurred. Colors indicate success rate during that session. **(b)** Example manual-control performance for six consecutive trials, 3 forward and 3 backward. World position is expressed in terms of the number of cycles of the pedal needed to move that distance. For plotting purposes, the position at the beginning of this stretch of behavior was set to zero. Bars indicate the time that targets turned on and off (horizontal span) and the size of the acceptance window (vertical span). **(c)** Similar plot during BMI control. For ease of comparison, world position is still expressed in terms of the number of physical cycles that would be needed to travel that far, although physical cycling no longer had any impact on virtual velocity. **(d)** Success rate for both monkeys. Each symbol plots, for one session, the proportion of trials where the monkey successfully moved from the initial target to the final target, stopped within it, and remained stationary until reward delivery. Dashed line at 1 for reference. **(e)** Target acquisition times for successful trials. Center lines indicate median, the box edges indicate the first and third quartiles, and the whiskers include all non-outlier points (points less than 1.5 times the interquartile range from the box edges). Data are shown separately for the three target distances. **(f)** Histograms of stopping location from both monkeys. Analysis considers both successful and failed trials. The bar at far right indicates the proportion of trials where the monkey failed for reasons other than stopping accuracy per se. This included trials where monkeys disrespected the reaction time limits, abandoned the trial before approaching the target, or passed through the target without stopping.

294   Performance was modestly better for monkey G versus E. This was likely due to the

295   implantation of two arrays rather than one. Work ethic may also have been a factor; monkey E

296   performed fewer trials under both BMI and manual control. Still, both monkeys could use the

297   BMI successfully starting on the first day, with success rates of 0.87 and 0.74 (monkey G and

298   E). Monkey G's performance rapidly approached his manual-control success rate within a few

299   sessions. Monkey E's performance also improved quickly, although his manual-control and

300   BMI-control success rates were mostly lower than Monkey G's. The last five sessions involved

301   BMI success rates of 0.97 and 0.96 for the two monkeys. This compares favorably with the

302   overall averages of 0.98 and 0.95 under manual control. Although this performance

303   improvement with time may relate to adaptation, the more likely explanation is simply that

304   monkeys learned to not be annoyed or discouraged by the small differences in decoded and

305   intended velocity.

306   ***State machine***

307   The performance documented above was achieved using a state-dependent decode (**Fig. 5**).

308   The angular-momentum-based strategy determined virtual self-motion (as described above)

309   when in the "STEADY" state. Thus, self-motion could be forward, backward, or stopped while

310   in STEADY. The use of other states was not strictly necessary but helped fine-tune

311   performance. State transitions were governed by activity in the moving-sensitive dimension,

312   which was translated into a probability of moving, p_{move} as described in the next section. If

313   p_{move} was low, the STOP state was active and decoded virtual velocity was enforced to be

314   zero. For those time-points when the STOP state was active, the angular-momentum-based

315   strategy would have typically estimated zero velocity even if it were not enforced.

316   Nevertheless, the use of an explicit STOP state was useful in nearly eliminating false starts. It

317   was also useful in detecting transitions from stopping to moving, allowing us to leverage the

318   initial-direction dimensions.

319   When p_{move} became high, the INIT state was entered but decoded velocity remained zero.

320   After 175 ms, the EARLY state was entered and velocity was decoded using the initial-direction

321   dimensions (see below). After an additional 200 ms, the STEADY state was entered. The

322   decode then depended only on the four rotational dimensions. Values of $p_{move} < 0.1$ always

323   produced a transition back to STOP. This typically occurred from STEADY to STOP, as the

324   movement was successfully ending. However, it could also occur from the other two states.
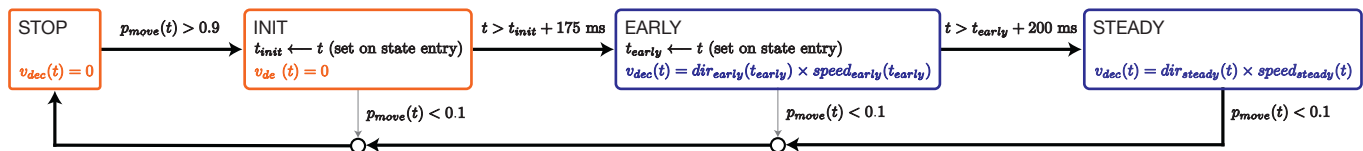
Figure 5. State machine diagram. BMI motion was determined by a state machine with four states: STOP, INIT, EARLY, and STEADY, corresponding to the different stages of a typical trial. The output of the state machine at every millisecond was an estimate of decoded velocity through the virtual environment, v_{dec}, which was then smoothed and integrated to compute virtual position. Black arrows indicate the typical path of a successful BMI trial and gray arrows indicate all other possible transitions. State transitions were governed by activity in the moving-sensitive dimension, which was translated into a probability of moving, p_{move}. While p_{move} was low, the STOP state was active and decoded velocity was set to zero. When p_{move} became high, the INIT state was entered but decoded velocity remained zero. If p_{move} remained high for 175 ms, the EARLY state was entered and velocity was decoded using the initial-direction dimensions. After another 200 ms, the STEADY state was entered and decoded velocity depended on the neural state in the rotational dimensions. If p_{move} dropped below 0.1 at any point, STOP was reentered. States in which progress is made through the virtual environment are highlighted in blue and states in which BMI motion is held at zero are highlighted in orange.

325   This was especially helpful if p_{move} became high very briefly (and presumably erroneously). In

326   such cases the state could transition from INIT back to STOP with the decoded velocity never

327   departing from zero.

Inferring the probability of moving

329   Decoders that directly translate neural state to cursor velocity have historically had difficulty

330   remaining stationary when there is no intended movement. The ability to successfully decode

331   stationarity is of even greater importance for self-motion. This was central to our motivation for

332   using a state machine with distinct stopped and moving states (Ethier et al., 2011; Kao et al.,

333   2017a; Kemere et al., 2008). To govern state transitions, we identified the moving-sensitive

334   dimension by applying linear discriminant analysis to the 50 training-data trials, and finding the

335   direction that best discriminated whether the monkey was moving versus stopped. Projecting

336   trial-averaged data onto that dimension (**Fig. 6a**) revealed that activity transitioned suddenly

337   from low to high just before movement onset, and back to low around the time movement

338   ended. This pattern was remarkably similar regardless of cycling direction (*red* and *green*

339   traces largely overlap). Activity in this dimension behaved similarly for single trials (**Fig. 6b**).

340   We used a Hidden Markov Model (HMM) (Kao et al., 2017a; Kemere et al., 2008) to estimate

341   p_{move}, which allows the current estimate to depend on all prior observations. Because those

342   observations must be independent, we did not use filtered rates (which were used for all other

343   aspects of the decode) but instead considered spike counts in non-overlapping bins, projected

344   onto the moving-sensitive dimension. Figure 6c plots the resulting distributions when stopped

345   (*orange*) and moving (*blue*). These overlapped modestly, a result of the narrow (10 ms) bin. The

346   estimate of p_{move} is robust to this overlap because the HMM leverages the full history of spike

347   counts; it can ignore brief weak evidence for moving while still transitioning swiftly given strong

348   evidence. During BMI control, p_{move} (**Fig. 6d**, *blue*) was typically near unity during intended

349   movement (i.e., when the monkey was actually cycling, *black*) and near zero otherwise.

350   Transitions both out of STOP and into STOP were determined by p_{move} (**Fig. 5**). We employed

351   a conservative design; entering a state that produced virtual movement required that p_{move}

352   exceed 0.9 and remain consistently above 0.1 for 175 ms. This led to a very low rate of false

353   starts (~2 per day for monkey G and ~1 every ten days for monkey E). The transition to EARLY

354   (**Fig. 6d**, left edge of *gray regions*) occurred on average 117 and 194 ms after physical

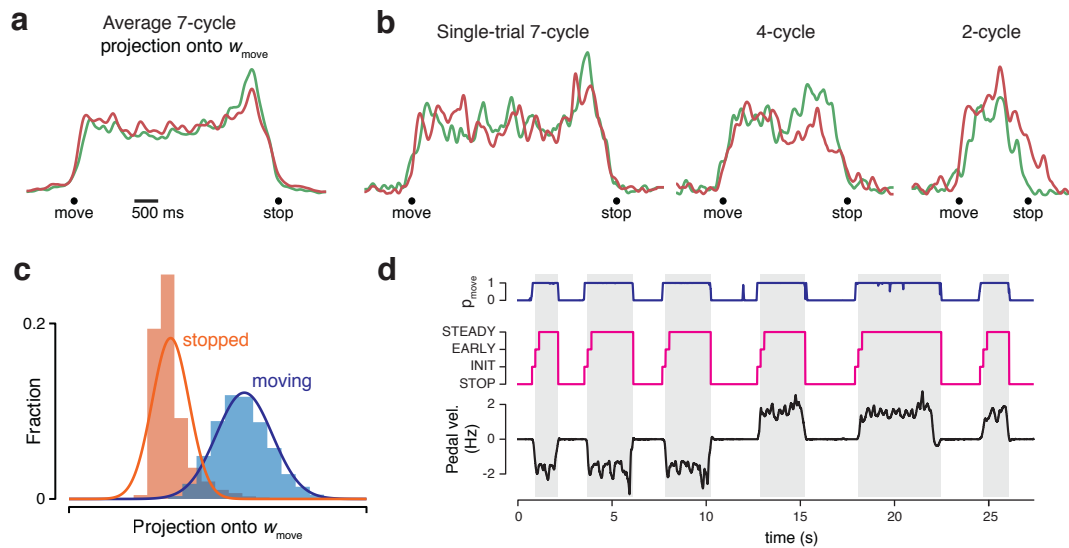355   movement onset (monkeys G and E). Trial-to-trial variability around these mean values was

Figure 6. Leveraging the moving-sensitive dimension to infer probability of moving. (a) Trial-averaged population activity, during a manual-control block, projected onto the moving-sensitive dimension (same session and trials as Figure 3a). **(b)** As in panel (a), but for three example single trials (same trials as in Figure 3b). **(c)** Histogram of the neural state projected onto the moving-sensitive dimension for training data. The neural state was measured every ten milliseconds, at times when the monkey was stopped within a target (*orange*) or actively cycling (*blue*). Traces show Gaussian fits used to compute p_{move}. **(d)** Example time-course, during BMI control, of p_{move} (*blue*) and the active state (*magenta*). Gray regions show times when the decoder produced virtual movement (i.e., when in EARLY or STEADY). These times corresponded well to times when the monkey was intending to move, as indicated by the angular velocity of the disconnected pedal (*black*). Note also that transient inappropriate spikes in p_{move} (as seen here around 18 s) do not lead to false starts because either they don't exceed 0.9, as was the case here, or they are too brief and the EARLY state is never reached. Same example data as in Figure 3c.

356   modest: standard deviations were 93 and 138 ms (computed within session and averaged

357   across sessions). As discussed above, estimated stopping time (when p_{move} dropped below

358   0.1) was also decoded with only modest trial-to-trial variability.

Inferring initial movement direction

360   Angular momentum of the neural state in the forward and backward planes became substantial

361   a few hundred milliseconds after p_{move} became high. Thus, the EARLY state became active

362   before the direction of movement could be inferred from the elliptical trajectories. To overcome

363   this problem, we leveraged the three-dimensional initial-direction subspace. The initial-

364   direction subspace comprised the top three PCs found from portions of the training data

365   surrounding movement onsets (a 200 ms segment from each trial, beginning at the time the

366   decoder would enter the INIT state, see *Methods*). The difference between the trajectory on

367   forward and backward trials began to grow just prior to physical movement onset, both on

368   average (**Fig. 7a**) and on individual trials (**Fig. 7b**; *solid* trajectory segment shows -200 to +175

369   ms relative to movement onset). For each of the 50 training trials, we considered the neural

370   state in these dimensions, measured 175 ms after decoded movement onset (**Fig. 7c**). We fit

371   Gaussian distributions separately for forward and backward trials.

372   During BMI control, upon transition from INIT to EARLY, we computed the likelihood of the

373   neural state under each distribution. A simple winner-take-all computation determined the

374   direction of virtual velocity during the EARLY state. The inference of movement direction during

375   EARLY was correct on 94% and 82% of trials (monkeys G and E). After 200 ms, the STEADY

376   state was entered and virtual velocity was controlled thereafter by activity in the rotational

377   dimensions. **Figure 7d** illustrates moments (*colored regions*) where the EARLY state was active

378   and the above strategy was used to decode virtual motion (physical pedal velocity is shown for

379   reference). These moments were brief, and had a very modest effect on the overall time to

380   reach the target. However, we still employed this strategy because our goal was to build a BMI

381   decode that closely tracked intended movement and felt responsive to the subject.

Speed control

383   The excellent performance of the decoder was aided by the relative simplicity of behavior:

384   when monkeys moved, they did so at a stereotyped speed. This allowed us to concentrate on

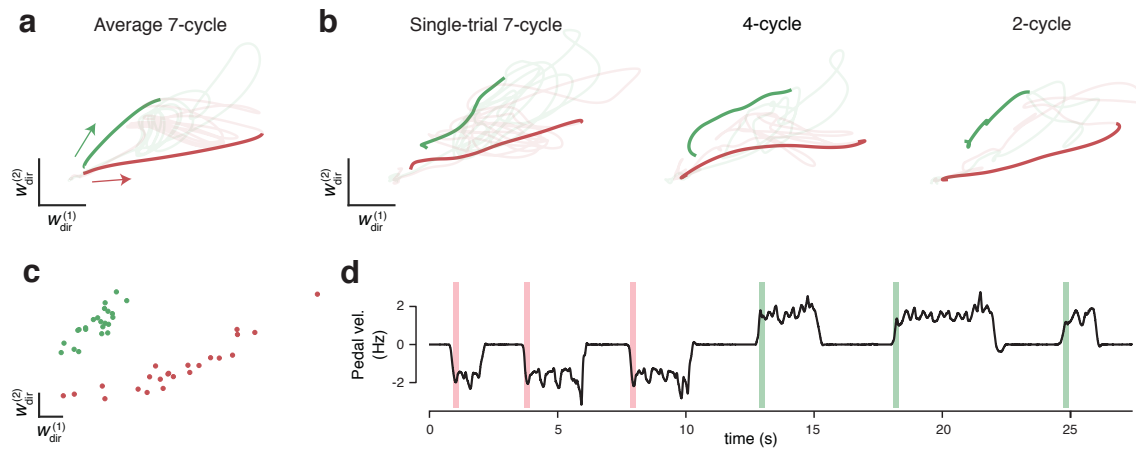385   building a decode algorithm that decoded intended direction with accurate timing, and

14

Figure 7. Leveraging initial-direction dimensions to allow low-latency decoding. (a) Trial-averaged population activity, during a manual-control block, projected onto two (of three) initial-direction dimensions (same session and trials as Figure 3a and 6a). Boldly colored portions of traces highlight -200 ms to +175 ms relative to physical move onset. Arrows indicate direction of trajectories. **(b)** As in panel (a), but for three example single trials (same trials as in Figure 3b and 6b). **(c)** The location of the neural state, for training data, at the time the state-machine (applied post-hoc to that training data) entered the EARLY state. This data (50 total trials) was used to fit two Gaussian distributions. During BMI control, when the EARLY state was entered, virtual direction was determined by which distribution maximized the data likelihood. **(d)** Example of initial-direction decoding during BMI control. Colored windows show the times in the EARLY state, with red and green indicating decoded direction. Same example data as in Figure 3c and 6d.

386 remained stationary if movement was not intended. However, that decode provided only

387 limited control of movement speed. An obvious extension is to allow finer-grained speed

388 control. This would presumably be desired by users of a self-motion prosthetic. Furthermore,

389 speed control provides one possible way of steering: e.g., by decoding the relative intensity of

390 intended movement on the two sides of the body. While we do not attempt that here, we still

391 considered it important to determine whether the neural features we identified could support

392 speed control.

393 That assessment required a task where speed control is necessary for success. We thus

394 trained one monkey to track various speed profiles as he progressed through the virtual

395 environment. Two floating targets were rendered in the foreground as the monkey cycled. The

396 distance between them reflected the difference between actual and instructed speed.

397 Obtaining juice required aligning the two floating targets while progressing towards a final

398 target, on which he stopped to obtain additional reward. The task was divided into trials, each

399 of which required moving a distance equivalent to twenty cycles under manual control. We

400 used eight trial-types, four each for forward and backward cycling. Two of these employed a

401 constant target speed (equivalent to 1 or 2 Hz cycling) and two involved a ramping speed (from

402 1 Hz to 2 Hz or vice versa). As above, the decoder was trained based on a small number of

403 manual-control trials performed at the beginning of each session. Blocks of manual-control

404 trials were also included for comparisons between manual and BMI-based performance.

405 Our decode strategy was largely preserved from that described above. However, we used a

406 modified state machine (**Supp. Fig. 1**) and a slightly different algorithm for transforming

407 rotations of the neural state into decoded virtual velocity. Direction was determined based on

408 which distribution (forward or backward) produced the higher likelihood of observing the

409 measured angular momentums (as in **Fig. 3d**). Once that choice was made, speed was

410 determined by the angular velocity of the neural state in that plane. Thus, faster rotational

411 trajectories led to faster decoded virtual velocity. We chose a scaling factor so that a given

412 neural angular velocity produced the speed that would have been produced by physical

413 cycling at that angular velocity. Neural angular velocity was exponentially filtered with a time

414 constant of 500 ms. The filter memory was erased on entry into a movement state (EARLY or

415 STEADY) from a stopped state (INIT or EXIT) to allow brisk movement onset (see *Methods)*.
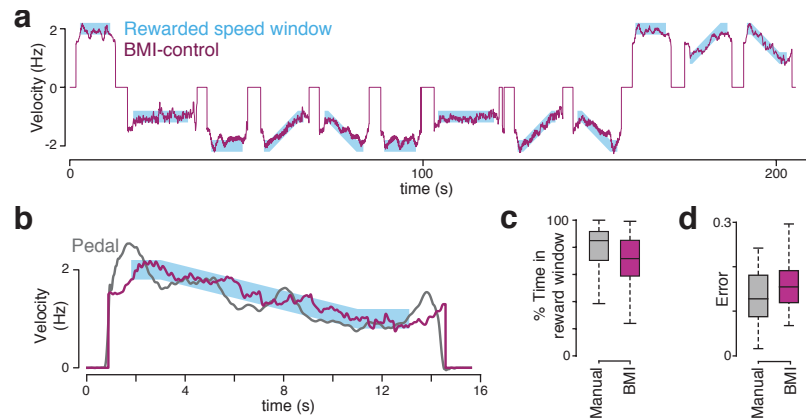
15

Figure 8. Performance in the modified task requiring speed tracking. (a) Instructed velocity and BMI-decoded virtual velocity during 12 contiguous trials of BMI control. **(b)** Expanded view of one example trial (the last trial from panel a). The virtual velocity that would have been produced by the pedal is shown in gray for comparison. **(c)** Percentage of time spent in rewarded velocity window for trials in manual-control (2 sessions, 333 trials) and BMI-control (3 sessions, 349 trials). Center lines indicate median, the box edges indicate the first and third quartiles, and the whiskers include all non-outlier points (points less than 1.5 times the interquartile range from the box edges). **(d)** Mean absolute error (MAE) between instructed velocity and virtual velocity for both manual control and BMI control sessions. One mean error was computed per trial. Same format as (c).

416   The above strategy allowed smooth BMI control of movement speed. In fact, it tended to give

417   BMI control an intrinsic advantage over manual control. In manual control, the angular velocity

418   of the pedal was naturally modulated within each cycle (being higher on the downstroke),

419   resulting in a fluctuating virtual velocity. Such fluctuations mildly impaired the ability to match

420   target speed under manual control. To allow a fair comparison, we thus also applied an

421   exponential filter to virtual velocity under manual control. Filters were chosen separately for

422   BMI ($\tau = 500$ ms) and manual control ($\tau = 1000$ ms) to maximize performance. This was done

423   informally, in the earliest session, by lengthening the filter until success rate roughly plateaued.

424   The filter then remained fixed for all further sessions.

425   Under BMI control, decoded virtual speed closely tracked instructed speed. This was true

426   across trials with different constant speeds, and within trials where speed modulated with time

427   (**Fig. 8a,b**). To compare BMI with manual control (which were performed on separate days) we

428   considered all trials where the monkey completed the portion of the trial that required matching

429   speed (87% of trials in arm control, and 79% in BMI control). The monkey was able to match

430   instructed speed nearly as accurately under BMI control as under manual control. This was

431   true judged both by time within the rewarded speed window (**Fig. 8c**) and by the error between

432   virtual and instructed velocity (**Fig. 8d**).

Discussion

Task-specific subspace decoding

435   We have previously argued that the largest signals in motor cortex are not 'representational' –

436   they do not encode variables but are instead essential for noise-robust dynamics. Those

437   dynamics produce outgoing commands that *are* representational (they covary with the

438   variables they control) but are low-variance. Because the dominant neural signals must be

439   produced by noise-robust dynamics, they obey the property of low trajectory tangling: similar

440   neural states avoid being associated with dissimilar derivatives (Russo et al., 2018). There is

441   little guarantee that the way in which low tangling is achieved will be the same across tasks –

442   on the contrary, the task often determines the most natural ways to keep tangling low. Thus,

443   the identity and number of high-variance dimensions will likely vary across tasks, as will the

444   basic response features captured by those dimensions. Put differently, both the intrinsic

445   covariance structure of the neural activity, and the nature of its correlations with kinematics,

446   will likely be task specific.

16

447   In this study we demonstrated that overtly task-specific decoding can be successful. This was

448   true even though we identified subspaces very differently from most reach-based BMI

449   approaches, and converted neural activity to movement using different (and often more non-

450   linear) approaches. These differences were critical. Unlike reaching we found no high-variance

451   dimensions where neural activity correlated with kinematics. Yet by using noncoding features

452   in high-variance dimensions, we achieved BMI control that was sufficiently natural that

453   monkeys appeared not to notice that the task was no longer under manual control. By most

454   measures (success rate, time to target) performance under BMI control was remarkably close

455   to that under manual control. The main limitation of BMI control was stopping accuracy.

456   Although our algorithm detected stopping with ~ 0.1 second precision, even small

457   discrepancies could lead to the target being over or undershot by a noticeable amount. A

458   beneficial feature of our BMI decode is that it almost never produced movement when it was

459   not intended. With rare exceptions, truly zero velocity was decoded when the monkey was

460   intending to remain stopped on the target. We consider this a particularly important attribute of

461   any self-motion decoding algorithm, due to the potentially large consequences of unintended

462   movement of the whole body.

463   ***Population dynamics in decoding***

464   The present approach relates to recent studies that modeled neural dynamics to improve

465   online (Kao et al., 2015) or offline (Aghagolzadeh and Truccolo, 2016; Gallego et al., 2020; Kao

466   et al., 2017b) decoding of movement kinematics. A key insight of those studies is that signals

467   that do not correlate directly with kinematics can be used to infer those that do. For linear

468   decoding, the value of a given variable depends upon the neural state in one dimension: the

469   dimension defined by the regression weights. Nevertheless, inferring the neural state in that

470   dimension may benefit from a dynamical model that spans multiple dimensions. Much like the

471   present approach, this allows the decode to leverage features that are robust, even if they do

472   not directly correlate with the kinematic parameters of interest. The present approach extends

473   this idea to situations where there may be no high-variance dimensions that can be linearly

474   decoded, and/or where the most prominent features are not well-described by linear dynamics.

475   Another way of leveraging additional dimensions – or even the full neural state – would be to

476   use a trained recurrent neural network (RNN) to decode parameters of interest (Sussillo et al.,

477   2012; Willett et al., 2020). This is a promising approach, but also has known drawbacks. For

478   safety in clinical implementation, it may be crucial to know which features the decoder is

17

479   actually exploiting, and to understand how it uses them. We therefore decided to work with

480   hand-selected features. While these features will not generalize to different tasks, that is in

481   some sense the point: the presence of task-specific covariance structure essentially ensures

482   that any decoding approach will need to be task-specific.

Self-motion BMIs

484   In choosing an alternative to traditional reach-based BMI tasks, we had three reasons for

485   focusing on a BMI for virtual self-motion. First, our recently developed cycling task naturally

486   lends itself to this application. Second, BMI-controlled self-motion is likely to be desired by a

487   large patient population (potentially much larger than the population that desires BMI-

488   controlled cursors or robot arms). Third, prior work has demonstrated that BMI control of self-

489   motion is viable (Libedinsky et al., 2016; Rajangam et al., 2016). In particular, Rajangam et al.

490   (Rajangam et al., 2016) demonstrated BMI control of a physical wheelchair based on neural

491   activity recorded from monkey motor and somatosensory cortex. Our work supports their

492   conclusion that BMI-controlled self-motion is possible, and demonstrates the feasibility of an

493   alternative decode strategy. Rajangam et al. employed a traditional decode strategy: linear

494   filters transformed neural activity into the key variables: translational and angular velocity. That

495   strategy allowed monkeys to navigate ~2 meters to a target (which had to be approached with

496   an accuracy of +/- ~0.2 meters, or 10% of the distance traveled) in an average of 27-49

497   seconds (depending on the monkey and degree of practice). In our task, monkeys had to stop

498   with similar relative accuracy: +/- 0.5 cycles, or 7% of the distance traveled for a seven-cycle

499   movement. They traversed those seven cycles in ~4 seconds under BMI control (averages of

500   4.3 and 3.7 seconds for monkey G and E). While this is roughly tenfold faster, we stress that

501   movement durations are not directly comparable between our task and theirs. Success

502   requirements differed in multiple ways. For example, Rajangam et al. required that monkeys

503   turn *en route* (which adds considerable challenge) but did not require them to stop on the

504   target location. Yet while direct comparison is not possible, a tenfold improvement in time-to-

505   target argues that task-specific subspace decode strategies can be effective and should be

506   explored further.

507   An obvious limitation of the current study is that we did not explore strategies for steering,

508   which would be essential to a real-world self-motion prosthetic. There exist multiple candidate

509   strategies for enabling steering. Rajangam et al. used a Wiener filter to decode angular velocity

510   of the body. While straightforward, this strategy appears to have had limited success: even

18

511   during training, the R^2 of their angular velocity decode was 0.16 and 0.12 for the two monkeys.

512   One alternative strategy would be to apply our decode strategy bilaterally, and employ a

513   comparison (e.g., between left and right cycling speed) to control angular velocity. This

514   strategy should be viable even with a unilateral implant; recent work has shown that

515   information about both forelimbs can be decoded equally well from either hemisphere (Ames

516   and Churchland, 2019; Heming et al., 2019). Another strategy would be to control translational

517   velocity using the strategies developed here, but use a reach-like decode for steering (rather

518   like pedaling a bicycle while also steering). Which (if any) of these three strategies is preferable

519   remains a question for future experiments.

Methods

520

521 *Subjects and primary task*

522 All procedures were approved by the Columbia University Institutional Animal Care and Use
523 Committee. Subjects G and E were two adult male macaque monkeys (*Macaca mulatta*).
524 Monkeys sat in a primate chair facing an LCD monitor (144 Hz refresh rate) that displayed a
525 virtual environment generated by the Unity engine (Unity Technologies, San Francisco, CA).
526 The head was restrained via a titanium surgical implant. While the monkey's left arm was
527 comfortably restrained, the right arm grasped a hand pedal. Cloth tape was used to ensure
528 consistent placement of the hand on the pedal. The pedal connected via a shaft to a motor
529 (Applied Motion Products, Watsonville, CA), which contained a rotary encoder that measured
530 the position of the pedal with a precision of 1/10,000 of the cycle. The motor was also used to
531 apply forces to the pedal, endowing it with virtual mass and viscosity.

532 Manual-control sessions for the primary cycling task required that the monkey cycle the pedal
533 in the instructed direction to move through the virtual environment, and stop on top of a lighted
534 target to collect juice reward. The color of the landscape indicated whether cycling must be
535 'forward' (green landscape, the hand moved away from the body at the top of the cycle) or
536 'backward' (tan landscape, the hand moved toward the body at the top of the cycle). There
537 were 6 total conditions, defined by cycling direction (forward or backward) and target distance
538 (2, 4, or 7 cycles). Distance conditions were randomized within same-direction blocks (3 trials
539 of each distance per block), and directional blocks were randomized over the course of each
540 experiment. Trials began with the monkey stationary on a target. A second target appeared in
541 the future. To obtain reward, the monkey had to cycle to that target, come to a halt 'on top' of
542 it (in the first-person perspective of the task) and remain stationary for a hold period of 1000-
543 1500 ms (randomized). A trial was aborted without reward if the monkey began moving before
544 target onset (or in the 170 ms after, which would indicate attempted anticipation), if the
545 monkey moved past the target without stopping, or if the monkey moved while awaiting
546 reward. The next trial began 100 ms after the variable hold period. Monkeys performed until
547 they received enough liquid reward that they chose to desist. As their motivation waned, they
548 would at times take short breaks. For both manual-control and BMI-control sessions, we
549 discarded any trials in which monkeys made no attempt to initiate the trial, and did not count
550 them as 'failed'. These trials occurred 2 ± 2 times per session (mean and standard deviation,
551 Monkey G, maximum 10) and 3 ± 3 times per session (Monkey E, maximum 11).

552 In BMI control, trial parameters and failure conditions were the same as in manual control, for
553 purposes of comparison. The only difference between manual and BMI control was that, in the
554 latter, position in the virtual environment was controlled by the output of a decoder rather than
555 the pedal. We did not prevent or discourage the monkey from cycling during BMI-control
556 blocks, and he continued to do so as normal. In BMI control, monkey G performed an average

557 of 654 trials/session over 20 sessions and monkey E performed an average of 137

558 trials/session over 17 sessions. Manual-control data for monkey G (average of 229

559 trials/session over 8 sessions) were collected during sessions in which BMI-control data sets

560 were also collected. Manual-control sessions for monkey E (average of 231 trials/session over

561 5 sessions) were interleaved with BMI-control sessions on different days. For monkey G, an

562 additional three manual-control sessions (189, 407, and 394 trials) were employed to record

563 EMG, which was used for the variance captured analysis (**Fig. 2**). We recorded from 5-7

564 muscles per session, yielding a total of 19 recordings. We made one or more recordings from

565 the three heads of the *deltoid*, the lateral and long heads of *triceps brachii*, the *biceps brachii*,

566 *trapezius,* and *latissimus dorsi*. These muscles were selected due to their clear activations

567 during the cycling task.

568 *Surgery and neural/muscle recordings*

569 Neural activity was recorded using chronic 96-channel Utah arrays (Blackrock Microsystems,

570 Salt Lake City, UT), implanted in the left hemisphere using standard surgical techniques. In

571 each monkey, an array was placed in the region of primary motor cortex (M1) corresponding to

572 the upper arm. In monkey G, a second array was placed in dorsal premotor cortex (PMd), just

573 anterior to the first array. Array locations were selected based on MRI scans and anatomical

574 landmarks observed during surgery. Experiments were performed 1-8 months (monkey G) and

575 3-4 months (monkey E) after surgical implantation. Neural responses both during the task and

576 during palpation confirmed that arrays were in the proximal-arm region of cortex.

577 Electrode voltages were filtered (band-pass 0.3 Hz – 7.5 kHz) and digitized at 30 kHz using

578 Digital Headstages, Digital Hubs, and Cerebus Neural Signal Processors from Blackrock

579 Microsystems. Digitized voltages were high-pass filtered (250 Hz) and spike events were

580 detected based on threshold crossings. Thresholds were set to between -4.5 and -3 times the

581 RMS voltage on each channel, depending on the array quality on a given day. On most

582 channels, threshold crossings included clear action-potential waveforms from one or more

583 neurons, but no attempt was made to sort action potentials.

584 Intra-muscular EMG recordings were made using pairs of hook-wire electrodes inserted with

585 30 mm x 27 gauge needles (Natus Neurology, Middleton, WI). Raw voltages were amplified and

586 filtered (band-pass 10 Hz – 10 kHz) with ISO-DAM 8A modules (World Precision Instruments,

587 Sarasota, FL), and digitized at 30 kHz with the Cerebus Neural Signal Processors. EMG was

588 then digitally band-pass filtered (50 Hz – 5 kHz) prior to saving for offline analysis. Offline, EMG

589 recordings were rectified, low-pass filtered by convolving with a Gaussian (standard deviation:

590 25 ms), downsampled to 1 kHz, and then fully normalized such that the maximum value

591 achieved on each EMG channel was 1.

592 A real-time target computer (Speedgoat, Bern, CH) running Simulink Real-Time environment

593 (MathWorks, Natick, MA) processed behavioral and neural data and controlled the decoder

21

594   output in online experiments. It also streamed variables of interest to another computer that
595   saved these variables for offline analysis. Stateflow charts were implemented in the Simulink
596   model to control task state flow as well as the decoder state machine. Real-time control had
597   millisecond precision.

598   Spike trains were causally converted to firing rates by convolving each spike with a beta kernel.
599   The beta kernel was defined by temporally scaling a beta distribution (shape parameters: $\alpha = 3$
600   and $\beta = 5$) to be defined over the interval [0, 275] ms and normalizing the kernel such that the
601   firing rates would be in units of spikes/second. The same filtering was applied for online
602   decoding and offline analyses. Firing rates were also mean centered (subtracting the mean rate
603   across all times and conditions) and normalized. During online decoding, the mean and
604   normalization factor were values that had been computed from the training data. We used soft
605   normalization (Russo et al., 2018): the normalization factor was the firing rate range plus a
606   constant (5 spikes/s).

607   *Computing trial-averaged firing rates*

608   Analyses of BMI performance are based on real-time decoding during online performance, with
609   no need to consider trial-averaged firing rates. However, we still wished to compute trial-
610   averaged traces of neural activity and kinematics for two purposes. First, some aspects of
611   decoder training benefited from analyzing trial-averaged firing rates. Second, we employ
612   analyses that document basic features of single-neuron responses and of the population
613   response (e.g., **Fig. 1d**, **Fig. 3a**, **Fig. 6a, Fig. 7a**). These analyses benefit from the denoising
614   that comes from computing a time-varying firing rate across many trials. Due to the nature of
615   the task, trials could be quite long (up to 20 cycles in the speed-tracking task), rendering the
616   traditional approach of aligning all trials to movement onset insufficient for preserving
617   alignment across all subsequent cycles. It was thus necessary to modestly adjust the time-
618   base of each individual trial (e.g., stretching time slightly for a trial where cycling was faster
619   than typical). We employed two alignment methods. Method A is a simplified procedure that
620   was used prior to parameter fitting when training the decoder before online BMI control. This
621   method aligns only times during the movement. Method B is a more sophisticated alignment
622   procedure that was utilized for all offline analyses. This method aligns the entire trial, including
623   pre- and post-movement data. For visualization, conditions with the same target distance (e.g.,
624   7 cycles), but different directions, were also aligned to the same time base. Critically, any data
625   processing that relied on temporal structure was completed in the original, unstretched time
626   base prior to alignment.

627   **Method A**: The world position for each trial resembles a ramp between movement onset and
628   offset (**Fig. 1a**). First, we identify the portion of each trial starting ¼ cycle into the movement
629   and ending ¼ cycle before the end of the movement. We fit a line to the world position in this
630   period and then extend that line until it intercepts the starting and ending positions. The data

631 between these two intercepts is considered the movement data for each trial and is extracted.
632 This movement data is then uniformly stretched in time to match the average trial length for
633 each trial's associated condition. This approach compresses slower than average movements
634 and stretches faster than average movements within a condition, such that they can be
635 averaged while still preserving many of the cycle-specific features of the data.

636 **Method B:** This method consists of a mild, non-uniform stretching of time in order to match
637 each trial to a condition-specific template. For complete details, see Russo et al. 2018. (Russo
638 et al., 2018)

639 *Variance captured analysis*

640 Analysis of neural variance captured (**Fig. 2**) was based on successful manual-control trials
641 from the three sessions with simultaneous neural and muscle recordings. We considered data
642 from the full duration of each trial, including times before movement onset and after movement
643 offset. We analyzed the variance captured by neural dimensions of three types. First, neural
644 dimensions where activity correlated strongly with kinematic features. Second, neural
645 dimensions where activity correlated strongly with muscle activity. Third, neural dimensions
646 that captured robust 'features' leveraged by our decoder.

647 Dimensions of the third type (were found as detailed below in a dedicated section below.
648 Dimensions of the first two types were found using the model $z(r,t) = c + \mathbf{w}^\top \mathbf{y}(r,t)$, where
649 $z(r,t)$ is the kinematic or muscle variable at time t during trial r, and $\mathbf{y}(r,t)$ is the
650 corresponding *N*-dimensional vector of neural firing rates. The constant c and the column
651 vector $\mathbf{w}$ were found via regression. The vector $\mathbf{w}$ defines a direction in neural space where
652 activity correlates strongly with the variable z. We found multiple such vectors; e.g. $\mathbf{w}_{x-vel}$ is a
653 dimension where neural activity correlates with horizontal velocity and $\mathbf{w}_{biceps}$ is a dimension
654 where neural activity correlates with biceps activity. All such vectors were scaled to have unity
655 norm before computing the neural variance captured by that dimension. Regression was based
656 on single-trial responses because this was intrinsically regularizing. We wished to encourage
657 regression to find high-variance dimensions if possible, and the use of single-trial data
658 encouraged it to do so. Because filtering of neural activity introduces a net lag, this analysis
659 naturally assumes a ~100 ms lag between neural activity and the variables of interest. Results
660 were extremely similar if we considered longer or shorter lags.

661 We wished to compute, for each dimension, the percentage of neural variance explained – i.e.,
662 whether that dimension captured large or small signals. We were not interested in whether
663 dimensions captured stochastic spiking variability, but in whether they captured large features
664 that were reliable across trials. Thus, variance captured was always computed based on trial-
665 averaged neural responses. We considered the matrix $\overline{Y} \in \mathbb{R}^{N \times T}$ where T is the total number of
666 time points across all conditions. Each row of $\overline{Y}$ contains the trial-averaged firing rate of one

23

667   neuron. We computed an $N \times N$ covariance matrix $\Sigma = \mathrm{cov}(\overline{Y})$ by treating rows of $\overline{Y}$ as random

668   variables and columns as observations. The proportion of total neural variance captured by a

669   given dimension, $\boldsymbol{w}$, is therefore:

670

$$\frac{\boldsymbol{w}^{\top}\Sigma\boldsymbol{w}}{\mathrm{tr}(\Sigma)}$$

671   Some analyses considered the variance captured by a subspace spanned by a set of

672   dimensions. To do so we took the sum of the variance captured by orthonormal dimensions

673   spanning that space.

674   *Decoding from kinematic dimensions*

675   Offline decodes **(Fig. 2c,d)** were performed using the same arm-control datasets described in

676   the previous section, but in this analysis the data were split into training and testing sets. The

677   training set for a session comprised the first 25 forward and 25 backward trials of that day (the

678   same training set size used in our online decodes). Regression dimensions were found for

679   these training sets as described above, and coefficients of determination were calculated on

680   the test sets.

681   *Identifying neural dimensions*

682   Although the response features leveraged by the decode algorithm are clearly visible in the top

683   principal components of the data (when PCA is performed on the full trial-averaged time-series

684   of firing rates across conditions), we sought to choose neural dimensions that would cleanly

685   isolate particular features. To this end, each feature was isolated using dedicated

686   preprocessing and dimensionality reduction approaches.

687   We sought a moving-sensitive dimension, the projection onto which would allow an HMM to

688   estimate the probability of moving, p_{move}, at each moment. To do so, we first computed binned

689   spike-counts (10 ms for monkey G, 20 ms for monkey E) and applied a square-root transform

690   to these counts as this has been shown to improve the Gaussian fit for Poisson data with small

691   counts (Thacker and Bromiley, 2001). We then aggregated all of these square-rooted binned

692   counts from the training set (25 forward trials, 25 backward trials) and separated them into two

693   classes based on pedaling speed: 'moving' (speed > 1 Hz) and 'stopped' (speed < .05 Hz).

694   Samples that didn't fall into either of these two classes were discarded. We applied linear

695   discriminant analysis to these two labeled sets, which yielded a discriminating hyperplane that

696   best separated the two classes. We defined the moving-sensitive dimension, $\boldsymbol{w}_{move}$, as the

697   vector normal to this hyperplane.

698   In order to decode direction, we sought to isolate four neural dimensions that captured

699   rotational trajectories during steady-state cycling. Spike time-series were filtered to yield firing

700   rates (as described above), and then further high-pass filtered (2nd order Butterworth, cutoff

24

701   frequency: 1 Hz). This removed drift or other low-frequency signals. Single-trial movement-

702   period responses were then aligned (Method A) and averaged within conditions to generate

703    $N \times T_c$ matrices $\overline{Y}_f$ and $\overline{Y}_b$. We sought a 4-dimensional projection of these trial-averaged

704   responses that would maximally capture rotational trajectories while segregating forward and

705   backward data into different planes. Whereas the standard PCA cost function finds dimensions

706   that maximize variance captured, we opted instead for a cost function that would maximize the

707   difference in variance captured between the two conditions:

708
$$J(W) = \mathrm{tr}(W^\top \Sigma_f W) - \mathrm{tr}(W^\top \Sigma_b W)$$

709   where $\Sigma_f = \mathrm{cov}(\overline{Y}_f)$, $\Sigma_b = \mathrm{cov}(\overline{Y}_b)$, W is constrained to be orthonormal. Note that this cost

710   function will be maximized when the projection of the data captures a great deal of variance for

711   forward trials and very little variance for backward trials. Conversely, this cost function will be

712   minimized when the projection favors large variances for backward trials and small variances

713   for forward trials. We thus chose to define our forward rotational plane by the 2D matrix $W_f =$

714    $\begin{bmatrix} \boldsymbol{w}_f^{(1)} & \boldsymbol{w}_f^{(2)} \end{bmatrix}$ that maximizes $J(W)$ and our backward rotational plane by the 2D matrix $W_b =$

715    $\begin{bmatrix} \boldsymbol{w}_b^{(1)} & \boldsymbol{w}_b^{(2)} \end{bmatrix}$ that minimizes $J(W)$. An iterative optimization procedure was used to find W_f and

716   W_b with the Manopt toolbox (Boumal et al., 2014); full details of this in (Cunningham and

717   Ghahramani, 2015).

718   To decode direction during the EARLY state, we found a set of initial-direction dimensions. We

719   used activity in the moving-sensitive dimension to determine the time, t_{init}, at which the state

720   machine would have entered the INIT state during online control. We then considered trial-

721   averaged neural activity, for each condition. from t_{init} through $t_{init} + 200$ ms. We applied PCA

722   and retained the top three dimensions: $\boldsymbol{w}_{dir}^{(1)}$, $\boldsymbol{w}_{dir}^{(2)}$, and $\boldsymbol{w}_{dir}^{(3)}$. Such dimensions capture how

723   activity evolves both across that timespan, and how it differs across forwards and backwards

724   cycling conditions.

725   *Computing probability of moving (p_{move})*

726   To compute p_{move} based on neural activity in the moving-sensitive dimension, an HMM was

727   used to track two states: 'moving' or 'stopped' (Kao et al., 2017a). Square-rooted spike counts

728   in the training data were already separated into 'moving' and 'stopped' sets for the purposes of

729   identifying $\boldsymbol{w}_{move}$. We projected those counts onto $\boldsymbol{w}_{move}$ and a fit Gaussian distribution for

730   each state. The probability, p_{move}, of being in the 'moving' state, given the entire sequence of

731   current and previously observed square-rooted spike counts, was computed efficiently with a

732   recursive algorithm that uses the state transition matrix

733
$$\Phi = \begin{bmatrix} p_{move|move} & p_{move|stop} \\ p_{stop|move} & p_{stop|stop} \end{bmatrix}$$

734 and knowledge of the Gaussian distributions. Φ encodes prior assumptions about the

735 probability of transitioning from one state to the next at any given bin. We used a benchmark

736 set of manual-control training data from each monkey to determine reasonable values for Φ,

737 which were then used in all experiments. For monkey G, we set $p_{move|stop} = .0001$ and

738 $p_{stop|move} = .002$; for monkey E, we set $p_{move|stop} = .0002$ and $p_{stop|move} = .004$. The value

739 p_{move} was used throughout the decoder state machine to control transitions between various

740 states, effectively dictating the movement onset and offset behavior of the decoder (**Fig. 6d**).

741 *Computing steady-state direction and speed*

742 Projecting single-trial, high-pass filtered firing rates onto the rotational planes spanned by W_f

743 and W_b yielded trajectories that differed considerably between forward and backward

744 conditions. To further denoise these state trajectories we applied a Kalman filter of the form

745
746
$$x_t = Ax_{t-1} + q_t$$
$$y_t = Cx_t + r_t$$

747 where $q_t \in \mathcal{N}(0, Q)$, and $r_t \in \mathcal{N}(0, R)$. In these equations, x_t represents the true underlying

748 neural state in the rotational dimensions and y_t are the high-pass filtered firing rates, which we

749 treat as noisy measurements of that underlying state. We chose to let our measurements be

750 smooth firing rates, rather than use non-overlapping bins of spikes, for purely opportunistic

751 reasons: it consistently yielded better performance by our decoder. The parameters of the

752 Kalman filter were fit to the training data as follows:

753
$$A = \overline{X}_2 \overline{X}_1^\top \left(\overline{X}_1 X_1^\top \right)^{-1}$$

754
$$C = \begin{bmatrix} W_f^\top \\ W_b^\top \end{bmatrix}^\dagger$$

755
$$Q = \mathrm{cov}(\overline{X}_2 - A\overline{X}_1)$$

756
$$R = \mathrm{cov}(Y - C\overline{X})$$

757 where

758
$$\overline{X}_1 = \begin{bmatrix} W_f^\top \\ W_b^\top \end{bmatrix} [\overline{Y}_f(:,1:T_f - 1), \overline{Y}_b(:,1:T_b - 1)]$$

759
$$\overline{X}_2 = \begin{bmatrix} W_f^\top \\ W_b^\top \end{bmatrix} [\overline{Y}_f(:,2:T_f), \overline{Y}_b(:,2:T_b)]$$

760
$$\overline{X} = \begin{bmatrix} W_f^\top \\ W_b^\top \end{bmatrix} [\overline{Y}_1, \overline{Y}_2, \dots, \overline{Y}_{50}]$$

761
$$Y = [Y_1, Y_2, \dots, Y_{50}]$$

762 with Y_i denoting the neural activity (high-pass filtered firing rates) for the i-th trial in the training

763 set, $\overline{Y}_i$ denoting the trial-averaged activity for the condition that the i-th trial is an instantiation

764 of, † denoting the Moore-Penrose pseudoinverse, and the colon symbol designating how to

765 index matrices (e.g., $M(:, a:b)$ refers to the submatrix of M including all rows of M, but only the

766 columns a through b). Lastly, the initial state parameter x_0 was computed by taking the

767 average value of the trial-averaged projections over all times and conditions. Online inference

768 of the underlying neural state, which yields an estimate $\hat{x}_t$ at each millisecond t, was computed

769 recursively using the steady-state form of the Kalman filter (Malik et al., 2011).

770 After denoising the neural state in the rotational dimensions via the Kalman filter, angular

771 momentum was computed in each plane as the cross product between the estimated neural

772 state and its derivative, which (up to a constant scaling) can be written

773
$$L(t) = \begin{bmatrix} L_f(t) \\ L_b(t) \end{bmatrix} = \begin{bmatrix} \hat{x}_{t-1}^{(1)}\hat{x}_t^{(2)} - \hat{x}_t^{(1)}\hat{x}_{t-1}^{(2)} \\ \hat{x}_{t-1}^{(3)}\hat{x}_t^{(4)} - \hat{x}_t^{(3)}\hat{x}_{t-1}^{(4)} \end{bmatrix}$$

774 where the superscript indexes the elements of $\hat{x}_t$. We fit 2D Gaussian distributions to these

775 angular momentums for each of three behaviors in the training data: 'stopped' (speed < .05

776 Hz), 'pedaling forward' (velocity > 1 Hz), and 'pedaling backward' (velocity < -1 Hz) (**Fig. 3d**).

777 Online, the likelihood of the observed angular momentums with respect to each of these three

778 distributions dictated the steady-state estimates of direction and speed. We'll denote these

779 three likelihoods f_{stop}, $f_{forward}$, and $f_{backward}$.

780 In general, one can compute which of these three distributions is most likely by choosing the

781 maximizing likelihood and assess confidence in that choice by comparing the relative values of

782 the three likelihoods. However, we wanted the decoder to err on the side of withholding

783 movement. We therefore set a conservative threshold on f_{stop} corresponding to the point at

784 which L would have a Mahalanobis distance of 3 to the stopped distribution of angular

785 momentums. If f_{stop} ever exceeded this threshold, we set $speed_{steady}$ to zero. If this condition

786 was not met, we decoded direction and speed as follows:

787
$$direction_{steady}(t) = \text{sgn}\left(f_{forward}(t) - f_{backward}(t)\right)$$

788
$$speed_{steady}(t) = \left| 2 \cdot \frac{f_{forward}(t)}{f_{forward}(t) + f_{backward}(t)} - 1 \right| \beta$$

789 where $\left| 2 \cdot \frac{f_{forward}(t)}{f_{forward}(t)+f_{backward}(t)} - 1 \right|$ varies between 0 and 1 depending on the relative sizes of

790 the likelihoods (yielding a slower velocity if the direction decode is uncertain) and β is a

791 direction-specific constant learned from the training data whose purpose is simply to scale up

792 the result to match steady-state cycling speed. In practice, $speed_{steady}$ was frequently very

793 close to the monkeys' steady-state cycling speeds (**Fig. 3e**).

794   *Computing initial direction and speed*

795   Initial direction and speed were always computed at the moment the EARLY state was entered,

796   t_{early}. These values then persisted throughout the remainder of the EARLY state. Given that

797   the decoder state machine doesn't make use of the initial-direction dimensions prior to

798   entering the EARLY state, t_{early} can be computed for the training trials. Single-trial firing rates

799   from the training set were then projected onto the initial-direction dimensions at t_{early} and 3D

800   Gaussian distributions were fit to the resulting sets of forward and backward neural states.

801   Online, firing rates were projected onto the initial-direction dimensions at t_{early} and likelihoods

802    $g_{forward}$ and $g_{backward}$ were computed with respect to each the learned distributions. If the

803   observed neural state in the initial-direction subspace was not an outlier (>10 Mahalanobis

804   distance units) with respect to both distributions, then the initial direction and speed were

805   computed as follows:

806
$$direction_{initial}(t_{early}) = \text{sgn}\left(g_{forward}(t_{early}) - g_{backward}(t_{early})\right)$$

807
$$speed_{initial}(t_{early}) = \left|2 \cdot \frac{g_{forward}(t_{early})}{g_{forward}(t_{early}) + g_{backward}(t_{early})} - 1\right|\beta$$

808   If the observed neural state was an outlier, initial direction and speed were computed in the

809   same manner as is done in the STEADY state.

810   *Smoothing of decoded velocity*

811   In the primary experiment, the decoder state machine produced an estimate of velocity, v_{dec},

812   at every millisecond. During the STOP and INIT states, this estimate was zero and the

813   monkey's position in the virtual environment was held constant. During the EARLY and

814   STEADY states, this estimate was smoothed with a trailing average:

815
$$v'_{dec}(t) = \frac{1}{T_{smooth} + 1} \sum_{i=0}^{T_{smooth}} v_{dec}(t - i)$$

816   where $T_{smooth} = \min(500, t - t_{early})$, i.e., the trailing average extended in history up to 500 ms

817   or to the moment the EARLY state was entered, whichever was shorter. v'_{dec} was integrated

818   every millisecond to yield decoded position in the virtual environment. In the speed-tracking

819   experiment (described below) there was no need to smooth of v_{dec} prior to integration because

820   the speed estimate had already been smoothed.

821   *Speed-tracking task*

822   In addition to the primary task (where the monkey traveled 2-7 cycles between stationary

823   targets) we employed a speed-tracking task, in which the monkey was required to match his

824   virtual speed to an instructed speed. Speed was instructed implicitly, via the relative position of

28

825   two moving targets. The primary target was located a fixed distance in front of the monkey's
826   location in virtual space: the secondary target fell 'behind' the first target when cycling was too
827   slow, and pulled 'ahead' if cycling was too fast. This separation saturated for large errors, but
828   for small errors was proportional to the difference between the actual and instructed speed.
829   This provided sufficient feedback to allow the monkey to track the instructed speed even when
830   it was changing. Because there was no explicit cue regarding the absolute instructed speed,
831   monkeys began cycling on each trial unaware of the true instructed speed profile and 'honed
832   in' on that speed over the first ~2 cycles.

833   We quantify instructed speed not in terms of the speed of translation through the virtual
834   environment (which has arbitrary units) but in terms of the physical cycling velocity necessary
835   to achieve the desired virtual speed. E.g., an instructed speed of 2 Hz necessitated cycling at
836   an angular velocity of 2 Hz to ensure maximal reward. Under BMI control, the output of the
837   decoder had corresponding units. For example, a 2 Hz angular velocity of the neural trajectory
838   produced movement at the same speed as 2 Hz physical cycling (see *'Neural features for*
839   *speed-tracking'* for details of decoder). Reward was given throughout the trial so long as the
840   monkey's speed was within 0.2 Hz of the instructed speed. We employed both constant and
841   ramping instructed-speed profiles.

842   Constant profiles were at either 1 Hz or 2 Hz. Trials lasted 20 cycles. After 18 cycles, the
843   primary and secondary targets (described above) disappeared and were replaced by a final
844   stationary target two cycles in front of the current position. Speed was not instructed during
845   these last two cycles; the monkey simply had to continue cycling and stop on the final target to
846   receive a large reward. Analyses of performance (e.g., **Fig. 8c,d**) were based on the ~16 cycle
847   period starting when the monkey first honed in on the correct speed (within 0.2 Hz of the
848   instructed speed) and ending when the speed-instructing cues disappeared 2 cycles before
849   the trial's end.

850   Ramping profiles began with three seconds of constant instructed speed to allow the monkey
851   to hone in on the correct initial speed. Instructed speed then ramped, over 8 seconds, to a new
852   value, and remained constant thereafter. As for constant profiles, speed-instructing cues
853   disappeared after 18 cycles and the monkey cycled two further cycles before stopping on a
854   final target. Again, analyses of performance were based on the period from when the monkey
855   first honed in on the correct speed, to when the speed-instructing cues disappeared. There
856   were two ramping profiles: one ramping up from 1 to 2 Hz, and one ramping down from 2 to 1
857   Hz. There were thus four total speed profiles (two constant and two ramping). These were
858   performed for both cycling directions (presented in blocks and instructed by color as in the
859   primary task) yielding eight total conditions. This task was only performed by monkey G, who
860   completed an average of 166 trials/session over 2 sessions in manual control and an average
861   of 116 trials/session over 3 sessions in BMI control.

862   As will be described below, the speed decoded during BMI control was low-pass filtered to
863   remove fluctuations due to noise. This had the potential to actually make the task easier under
864   BMI control, given that changes in instructed speed were slow within a trial (excepting the
865   onset and offset of movement). We did not wish to provide BMI control with an 'unfair'
866   advantage in comparisons with manual control. We therefore also low-pass filtered virtual
867   speed while under manual control. Filtering (exponential, τ = 1 second) was applied only when
868   speed was above 0.2 Hz, so that movement onset and offset could remain brisk. This aided the
869   monkey's efforts to track slowly changing speeds under manual control.

870   During training and while under manual control, trials were failed if there was ever a large
871   discrepancy between actual and instructed speed. This ensured that monkeys tried their best
872   to consistently match speed at all times. We relaxed this failure mode under BMI control
873   because we did not wish to mask large failures in decoded speed. Over the course of single
874   sessions, this did not discourage monkeys from trying their best, but simply allowed us to
875   observe and quantify decode failures that would otherwise have resulted in aborted trials. This
876   potentially puts BMI performance – quantified as in **Figure 8c,d** – at a disadvantage relative to
877   manual control, where large errors could not persist. In practice this was not an issue as large
878   errors were rare.

879   *Neural features for speed-tracking*

880   Although the speed-tracking experiment leveraged the same dominant neural responses that
881   were used in the primary experiment, the specific features calculated for the decoder state
882   machines differed. Details on how the relevant features were calculated in the speed-tracking
883   experiment are presented in this section.

884   The probability of moving, p_{move}, was calculated using a different set of parameters for speed-
885   tracking, largely due to changes in recording quality in the intervening time between data
886   collection from the primary experiment and data collection for the speed-tracking experiment.
887   The bin size was increased to 100 ms and the following state transition values were used:
888    $p_{move|stop}$ = .0005 and $p_{stop|move}$ = .0005. In addition, we observed that the square-root
889   transform seemed to be having a negligible impact on the quality of the decoder at this bin
890   size, so we removed it for this task.

891   Several features used in the speed-tracking state machine rely on neural activity in the
892   rotational dimensions. In the primary experiment, this activity was high-pass filtered (cutoff
893   frequency: 1 Hz) prior to projection into these dimensions, which helped isolate the rotational
894   neural trajectories during ~2 Hz cycling. For speed-tracking, we wanted to accommodate a
895   broader range of cycling speeds (which corresponded to a broader range of periodicities in the
896   rotational neural trajectories). Thus, we dropped the cutoff frequency from 1 Hz to 0.75 Hz for
897   this experiment.

898 In computing $direction_{steady}$, the same computations were performed as for the primary-

899 experiment, with one exception: a new direction was not necessarily decoded every

900 millisecond. In order to decode a new direction, the follow conditions needed to be met: 1) the

901 observed angular momentums had a Mahalanobis distance of less than 4 to the distribution

902 corresponding to the decoded direction, 2) the observed angular momentums had a

903 Mahalanobis distance of greater than 6 to the distribution corresponding to the opposite

904 direction. These criteria ensured that a new steady-state direction was only decoded when the

905 angular momentums were highly consistent with a particular direction. When these criteria

906 were not met, the decoder continued to decode the same direction from the previous time

907 step.

908 Speed was computed identically in the EARLY and STEADY states by decoding directly from

909 the rotational plane corresponding to the decoded direction. A coarse estimate of speed was

910 calculated as the derivative of the phase of rotation follows:

911
$$\theta'(t) = \begin{cases} \dfrac{d\theta_f}{dt}, & direction(t) = +1 \\ \dfrac{d\theta_b}{dt}, & direction(t) = -1 \end{cases}$$

912 where $\theta_f(t)$ and $\theta_b(t)$ are the phases of the two planes in the neural state estimate $\hat{x}_t$,

913 $direction$ corresponds to $direction_{early}$ while in the EARLY state and $direction_{steady}$ while in

914 the STEADY state, and the derivative θ' is computed in units of Hz. The coarse speed estimate,

915 θ', was then smoothed with an exponential moving average (τ = 500 ms) to generate $speed$, the

916 variable that gets used in the decoder state machine. Additional saturation limits were set such

917 that $speed$ never dropped below 0.5 Hz or exceeded 3.5 Hz, so as to remain in the range

918 typically seen during pedaling. On entry into EARLY or STEADY from either INIT or EXIT, when

919 $speed$ gets initialized, the output of this exponential moving average was reset to an initial

920 value of 1.5 Hz, which was the average starting speed across conditions.

921 Lastly, there were two new conditions for decoder state transitions in the speed-tracking

922 experiment (**Supp. Fig. 1**). First, transitions from INIT to EARLY required that a condition

923 termed "confident initial direction decode" was obtained. This condition was met when the

924 Mahalanobis distance from the neural state in the initial-direction subspace to either the

925 forward or backward distributions dropped below 4. Second, transitions into the EXIT state

926 required (in addition to a drop in p_{move}) that the observed angular momentums, L, belong to a

927 set termed 'Stationary'. This set was defined as all L with a Mahalanobis distance of less than

928 4 to the 'stopped' distribution of angular momentums, which was learned from the training set.

929

930

31
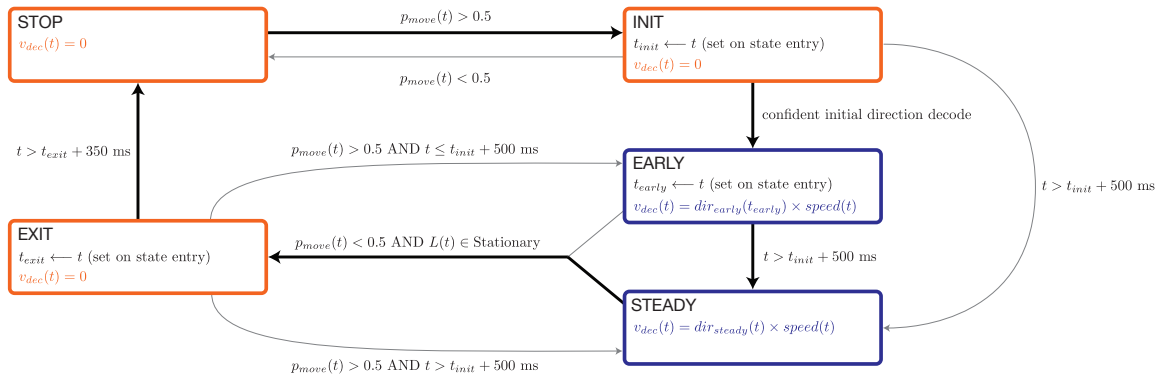
Supplementary Figure 1. State machine diagram for speed-control experiments. BMI motion for the speed-tracking experiment was determined by a state machine with five states: STOP, INIT, EARLY, STEADY, and EXIT. Each of these states describes how to compute virtual velocity, v_{dec}, which gets integrated every millisecond into virtual position. Following the conventions from Figure 4, black arrows indicate the typical path of a successful BMI trial (gray arrows indicate all other transitions) and colors differentiate states in which there is progress through the virtual environment (blue) from states in which BMI motion is zero (orange). In the STOP, INIT, and EXIT states, virtual velocity is simply set to zero. During the EARLY and STEADY states, virtual velocity is computed as the product of decoded direction and decoded speed, which are computed based on activity in the rotational dimensions. Transitions between the states were determined by p_{move} (computed from the moving-sensitive dimension), angular momentum vector L (computed from the rotational planes), and the neural state in the initial-direction dimensions. Details on computing each of the neural features used in this state machine are provided in the section *'Neural features for speed-tracking'*. While in the STOP state, virtual velocity remains zero. If p_{move} goes high, the INIT state is entered (time of entry is denoted t_{init}), but virtual velocity remains zero. From the INIT state, one of three things can happen: 1) p_{move} goes low and the movement aborts with a transition back to the STOP state, 2) the neural state in the initial-direction dimensions becomes sufficiently close to the learned distributions of neural states for forward or backward conditions, triggering a transition to the EARLY state, or 3) no transition occurs within 500 ms of t_{init}, triggering a transition to the STEADY state. The INIT state serves to withhold BMI motion in situations where there is a transient spike in p_{move} and to delay movement when the early estimate of decoded direction is only weakly confident. The EARLY state dictates how virtual velocity is computed in the early portion of movement (when less than 500 ms have elapsed since t_{init}). The STEADY state determines virtual velocity for the remainder of decoded movement. While in the EARLY or STEADY states, if p_{move} goes low and the angular momentums in the rotational planes are consistent with a stationary pedal, a transition will occur to the EXIT state and virtual velocity will again go to zero. After 350 consecutive ms in the EXIT state, the state machine transitions back to the STOP state. However, if p_{move} goes high while in the EXIT state, a transition back to either EARLY or STEADY will occur. The transitions from EXIT back to EARLY and STEADY

exist to allow a rapid return to decoded movement if neural activity briefly, erroneously reflects that the monkey is ceasing movement, but then returns to exhibiting robust activity consistent with an ongoing movement.

Supplementary Movie 1. MI and manual control of primary task (monkey G, 10/4/2018). Both manual (left) and BMI control (right) sessions were performed on the same day, which was the fourth day of BMI control. Manual and BMI control success rates were very similar on this day (see Figure 3d). The task required that the monkey turn the hand pedal in the instructed direction to move through the virtual environment, stop on top of a lighted target, and remain still while collecting juice reward. The color of the landscape indicated whether cycling must be 'forward' (green landscape) or 'backward' (tan landscape). There were 6 total conditions, defined by cycling direction and target distance (2, 4, or 7 cycles).

Supplementary Movie 2. BMI and manual control of speed-tracking task (monkey G, 4/18/2019 and 3/27/2019, respectively). These examples were selected as representative of performance in this task. In this version of the task, the monkey was required to track various instructed speed profiles (constant, ramping up, and ramping down) as he progressed through the environment. A red target was rendered a short distance in front of the monkey, and remained at that distance ahead throughout the trial. A second, white target drifted ahead or behind the red target to indicate the error between the avatar's speed and the instructed speed. Thus, successful speed tracking required aligning these targets on top of one another. Whenever the error was within the rewarded tolerance window, the white target would light up and juice reward would be dispensed. This speed-tracking epoch lasted until the monkey was within two cycles of the final turquoise stopping target (total of 20 cycles from starting position).

Author Contributions

M.M.C. conceived the study. K.E.S., S.M.P., and M.M.C. designed experiments. S.M.P., K.E.S., M.M.C., and Q.W. created the decoding algorithms. K.E.S. and S.M.P. collected and analyzed datasets. K.E.S., S.M.P., and M.M.C. wrote the paper. All authors contributed to editing.

References

Aghagolzadeh M, Truccolo W. 2016. Inference and Decoding of Motor Cortex Low-Dimensional Dynamics via Latent State-Space Models. *IEEE Trans Neural Syst Rehabil Eng* **24**:272–282. doi:10.1109/TNSRE.2015.2470527

Ajiboye AB, Willett FR, Young DR, Memberg WD, Murphy BA, Miller JP, Walter BL, Sweet JA, Hoyen HA, Keith MW, Peckham PH, Simeral JD, Donoghue JP, Hochberg LR, Kirsch RF. 2017. Restoration of reaching and grasping movements through brain-controlled muscle stimulation in a person with tetraplegia: a proof-of-concept demonstration. *The Lancet* **0**. doi:10.1016/S0140-6736(17)30601-3

Ames KC, Churchland MM. 2019. Motor cortex signals for each arm are mixed across hemispheres and neurons yet partitioned within the population response. *eLife* **8**. doi:10.7554/eLife.46159

Boumal N, Mishra B, Absil P-A, Sepulchre R. 2014. Manopt, a Matlab Toolbox for Optimization on Manifolds. *J Mach Learn Res* **15**:1455–1459.

Carmena JM, Lebedev MA, Crist RE, O'Doherty JE, Santucci DM, Dimitrov DF, Patil PG, Henriquez CS, Nicolelis MAL. 2003. Learning to Control a Brain–Machine Interface for Reaching and Grasping by Primates. *PLoS Biol* **1**:e42. doi:10.1371/journal.pbio.0000042

Chapin JK, Moxon KA, Markowitz RS, Nicolelis MAL. 1999. Real-time control of a robot arm using simultaneously recorded neurons in the motor cortex. *Nat Neurosci* **2**:664–670. doi:10.1038/10223

Christie BP, Tat DM, Irwin ZT, Gilja V, Nuyujukian P, Foster JD, Ryu SI, Shenoy KV, Thompson DE, Chestek CA. 2014. Comparison of spike sorting and thresholding of voltage waveforms for intracortical brain–machine interface performance. *J Neural Eng* **12**:016009. doi:10.1088/1741-2560/12/1/016009

Churchland MM, Cunningham JP, Kaufman MT, Foster JD, Nuyujukian P, Ryu SI, Shenoy KV. 2012. Neural population dynamics during reaching. *Nature* **487**:51–56. doi:10.1038/nature11129

Churchland MM, Shenoy KV. 2007. Temporal complexity and heterogeneity of single-neuron activity in premotor and motor cortex. *J Neurophysiol* **97**:4235–4257. doi:10.1152/jn.00095.2007

Churchland MM, Yu BM, Sahani M, Shenoy KV. 2007. Techniques for extracting single-trial activity patterns from large-scale neural recordings. *Curr Opin Neurobiol*, Neuronal and glial cell biology / New technologies **17**:609–618. doi:10.1016/j.conb.2007.11.001

Collinger JL, Wodlinger B, Downey JE, Wang W, Tyler-Kabara EC, Weber DJ, McMorland AJ, Velliste M, Boninger ML, Schwartz AB. 2013. 7 degree-of-freedom neuroprosthetic control by an individual with tetraplegia. *Lancet* **381**:557–564. doi:10.1016/S0140-6736(12)61816-9

Cunningham JP, Ghahramani Z. 2015. Linear Dimensionality Reduction: Survey, Insights, and Generalizations. *J Mach Learn Res* **16**:2859–2900.

Degenhart AD, Bishop WE, Oby ER, Tyler-Kabara EC, Chase SM, Batista AP, Yu BM. 2020. Stabilization of a brain–computer interface via the alignment of low-dimensional spaces of neural activity. *Nat Biomed Eng* **4**:672–685. doi:10.1038/s41551-020-0542-9

Elsayed GF, Lara AH, Kaufman MT, Churchland MM, Cunningham JP. 2016. Reorganization between preparatory and movement population responses in motor cortex. *Nat Commun* **7**. doi:10.1038/ncomms13239

Ethier C, Oby ER, Bauman MJ, Miller LE. 2012. Restoration of grasp following paralysis through brain-controlled stimulation of muscles. *Nature* **485**:368–371. doi:10.1038/nature10987

Ethier C, Sachs NA, Miller LE. 2011. Continuous state-dependent decoders for brain machine interfaces2011 5th International IEEE/EMBS Conference on Neural Engineering. Presented at the 2011 5th International IEEE/EMBS Conference on Neural Engineering. pp. 473–477. doi:10.1109/NER.2011.5910589

Fernández-Rodríguez Á, Velasco-Álvarez F, Ron-Angevin R. 2016. Review of real brain-controlled wheelchairs. *J Neural Eng* **13**:061001. doi:10.1088/1741-2560/13/6/061001

Fetz EE, Finocchio DV, Baker MA, Soso MJ. 1980. Sensory and motor responses of precentral cortex cells during comparable passive and active joint movements. *J Neurophysiol* **43**:1070–1089.

Gallego JA, Perich MG, Chowdhury RH, Solla SA, Miller LE. 2020. Long-term stability of cortical population dynamics underlying consistent behavior. *Nat Neurosci* **23**:260–270. doi:10.1038/s41593-019-0555-4

Gallego JA, Perich MG, Miller LE, Solla SA. 2017. Neural Manifolds for the Control of Movement. *Neuron* **94**:978–984. doi:10.1016/j.neuron.2017.05.025

Gallego JA, Perich MG, Naufel SN, Ethier C, Solla SA, Miller LE. 2018. Cortical population activity within a preserved neural manifold underlies multiple motor behaviors. *Nat Commun* **9**:4233. doi:10.1038/s41467-018-06560-z

Gilja V, Nuyujukian P, Chestek CA, Cunningham JP, Yu BM, Fan JM, Churchland MM, Kaufman MT, Kao JC, Ryu SI, Shenoy KV. 2012. A high-performance neural prosthesis enabled by control algorithm design. *Nat Neurosci* **15**:1752–1757. doi:10.1038/nn.3265

Gilja V, Pandarinath C, Blabe CH, Nuyujukian P, Simeral JD, Sarma AA, Sorice BL, Perge JA, Jarosiewicz B, Hochberg LR, Shenoy KV, Henderson JM. 2015. Clinical translation of a high-performance neural prosthesis. *Nat Med* **21**:1142–1145. doi:10.1038/nm.3953

Golub MD, Sadtler PT, Oby ER, Quick KM, Ryu SI, Tyler-Kabara EC, Batista AP, Chase SM, Yu BM. 2018. Learning by neural reassociation. *Nat Neurosci* 1. doi:10.1038/s41593-018-0095-3

Heming EA, Cross KP, Takei T, Cook DJ, Scott SH. 2019. Independent representations of ipsilateral and contralateral limbs in primary motor cortex. *eLife* **8**:e48190. doi:10.7554/eLife.48190

Kao JC, Nuyujukian P, Ryu SI, Churchland MM, Cunningham JP, Shenoy KV. 2015. Single-trial dynamics of motor cortex and their applications to brain-machine interfaces. *Nat Commun* **6**:1–12. doi:10.1038/ncomms8759

Kao JC, Nuyujukian P, Ryu SI, Shenoy KV. 2017a. A High-Performance Neural Prosthesis Incorporating Discrete State Selection With Hidden Markov Models. *IEEE Trans Biomed Eng* **64**:935–945. doi:10.1109/TBME.2016.2582691

Kao JC, Ryu SI, Shenoy KV. 2017b. Leveraging neural dynamics to extend functional lifetime of brain-machine interfaces. *Sci Rep* **7**. doi:10.1038/s41598-017-06029-x

Kaufman MT, Churchland MM, Ryu SI, Shenoy KV. 2014. Cortical activity in the null space: permitting preparation without movement. *Nat Neurosci* **17**:440–448. doi:10.1038/nn.3643

Kaufman MT, Seely JS, Sussillo D, Ryu SI, Shenoy KV, Churchland MM. 2016. The Largest Response Component in the Motor Cortex Reflects Movement Timing but Not Movement Type. *eNeuro* **3**. doi:10.1523/ENEURO.0085-16.2016

Kemere C, Santhanam G, Yu BM, Afshar A, Ryu SI, Meng TH, Shenoy KV. 2008. Detecting Neural-State Transitions Using Hidden Markov Models for Motor Cortical Prostheses. *J Neurophysiol* **100**:2441–2452. doi:10.1152/jn.00924.2007

Lemon RN, Hanby JA, Porter R. 1976. Relationship between the activity of precentral neurones during active and passive movements in conscious monkeys. *Proc R Soc Lond B Biol Sci* **194**:341–373. doi:10.1098/rspb.1976.0083

Libedinsky C, So R, Xu Z, Kyar TK, Ho D, Lim C, Chan L, Chua Y, Yao L, Cheong JH, Lee JH, Vishal KV, Guo Y, Chen ZN, Lim LK, Li P, Liu L, Zou X, Ang KK, Gao Y, Ng WH, Han BS, Chng K, Guan C, Je M, Yen S-C. 2016. Independent Mobility Achieved through a Wireless Brain-Machine Interface. *PLOS ONE* **11**:e0165773. doi:10.1371/journal.pone.0165773

Makin JG, O'Doherty JE, Cardoso MMB, Sabes PN. 2018. Superior arm-movement decoding from cortex with a new, unsupervised-learning algorithm. *J Neural Eng* **15**:026010. doi:10.1088/1741-2552/aa9e95

Malik WQ, Truccolo W, Brown EN, Hochberg LR. 2011. Efficient Decoding With Steady-State Kalman Filter in Neural Interface Systems. *IEEE Trans Neural Syst Rehabil Eng* **19**:25–34. doi:10.1109/TNSRE.2010.2092443

Michaels JA, Dann B, Scherberger H. 2016. Neural Population Dynamics during Reaching Are Better Explained by a Dynamical System than Representational Tuning. *PLOS Comput Biol* **12**:e1005175. doi:10.1371/journal.pcbi.1005175

Miri A, Warriner CL, Seely JS, Elsayed GF, Cunningham JP, Churchland MM, Jessell TM. 2017. Behaviorally Selective Engagement of Short-Latency Effector Pathways by Motor Cortex. *Neuron* **95**. doi:10.1016/j.neuron.2017.06.042

Pruszynski JA, Kurtzer I, Nashed JY, Omrani M, Brouwer B, Scott SH. 2011. Primary motor cortex underlies multi-joint integration for fast feedback control. *Nature* **478**:387–390. doi:10.1038/nature10436

Rajangam S, Tseng P-H, Yin A, Lehew G, Schwarz D, Lebedev MA, Nicolelis MAL. 2016. Wireless Cortical Brain-Machine Interface for Whole-Body Navigation in Primates. *Sci Rep* **6**. doi:10.1038/srep22170

Russo AA, Bittner SR, Perkins SM, Seely JS, London BM, Lara AH, Miri A, Marshall NJ, Kohn A, Jessell TM, Abbott LF, Cunningham JP, Churchland MM. 2018. Motor Cortex Embeds Muscle-like Commands in an Untangled Population Response. *Neuron* **97**:953-966.e8. doi:10.1016/j.neuron.2018.01.004

Sadtler PT, Quick KM, Golub MD, Chase SM, Ryu SI, Tyler-Kabara EC, Yu BM, Batista AP. 2014. Neural constraints on learning. *Nature* **512**:423–426. doi:10.1038/nature13665

Schroeder KE, Irwin ZT, Bullard AJ, Thompson DE, Bentley JN, Stacey WC, Patil PG, Chestek CA. 2017. Robust tactile sensory responses in finger area of primate motor cortex relevant to prosthetic control. *J Neural Eng* **14**:046016. doi:10.1088/1741-2552/aa7329

Scott SH, Gribble PL, Graham KM, Cabel DW. 2001. Dissociation between hand motion and population vectors from neural activity in motor cortex. *Nature* **413**:161–165. doi:10.1038/35093102

Sergio LE, Hamel-Pâquet C, Kalaska JF. 2005. Motor Cortex Neural Correlates of Output Kinematics and Kinetics During Isometric-Force and Arm-Reaching Tasks. *J Neurophysiol* **94**:2353–2378. doi:10.1152/jn.00989.2004

Serruya MD, Hatsopoulos NG, Paninski L, Fellows MR, Donoghue JP. 2002. Brain-machine interface: Instant neural control of a movement signal. *Nature* **416**:141–142. doi:10.1038/416141a

Shanechi MM, Orsborn AL, Moorman HG, Gowda S, Dangi S, Carmena JM. 2017. Rapid control and feedback rates enhance neuroprosthetic control. *Nat Commun* **8**:13825. doi:10.1038/ncomms13825

Shenoy KV, Carmena JM. 2014. Combining Decoder Design and Neural Adaptation in Brain-Machine Interfaces. *Neuron* **84**:665–680. doi:10.1016/j.neuron.2014.08.038

Shenoy KV, Sahani M, Churchland MM. 2013. Cortical control of arm movements: A dynamical systems perspective. *Annu Rev Neurosci* **36**:337–359. doi:10.1146/annurev-neuro-062111-150509

Suminski AJ, Tkach DC, Hatsopoulos NG. 2009. Exploiting multiple sensory modalities in brain-machine interfaces. *Neural Netw* **22**:1224–1234. doi:10.1016/j.neunet.2009.05.006

Sussillo D, Churchland MM, Kaufman MT, Shenoy KV. 2015. A neural network that finds a naturalistic solution for the production of muscle activity. *Nat Neurosci* **18**:1025–1033. doi:10.1038/nn.4042

Sussillo D, Nuyujukian P, Fan JM, Kao JC, Stavisky SD, Ryu S, Shenoy K. 2012. A recurrent neural network for closed-loop intracortical brain–machine interface decoders. *J Neural Eng* **9**:026027. doi:10.1088/1741-2560/9/2/026027

Sussillo D, Stavisky SD, Kao JC, Ryu SI, Shenoy KV. 2016. Making brain–machine interfaces robust to future neural variability. *Nat Commun* **7**:13749. doi:10.1038/ncomms13749

Taylor DM, Tillery SIH, Schwartz AB. 2002. Direct Cortical Control of 3D Neuroprosthetic Devices. *Science* **296**:1829–1832. doi:10.1126/science.1070291

Thacker NA, Bromiley PA. 2001. The Effects of a Square Root Transform on a Poisson Distributed Quantity. (Technical Report). Manchester, UK: Univ. of Manchester.

Trautmann EM, Stavisky SD, Lahiri S, Ames KC, Kaufman MT, O'Shea DJ, Vyas S, Sun X, Ryu SI, Ganguli S, Shenoy KV. 2019. Accurate Estimation of Neural Population Dynamics without Spike Sorting. *Neuron* **0**. doi:10.1016/j.neuron.2019.05.003

Velliste M, Perel S, Spalding MC, Whitford AS, Schwartz AB. 2008. Cortical control of a prosthetic arm for self-feeding. *Nature* **453**:1098–1101. doi:10.1038/nature06996

Wessberg J, Stambaugh CR, Kralik JD, Beck PD, Laubach M, Chapin JK, Kim J, Biggs SJ, Srinivasan MA, Nicolelis MAL. 2000. Real-time prediction of hand trajectory by ensembles of cortical neurons in primates. *Nature* **408**:361–365. doi:10.1038/35042582

Willett FR, Avansino DT, Hochberg LR, Henderson JM, Shenoy KV. 2020. High-performance brain-to-text communication via imagined handwriting. *bioRxiv* 2020.07.01.183384. doi:10.1101/2020.07.01.183384

Wodlinger B, Downey JE, Tyler-Kabara EC, Schwartz AB, Boninger ML, Collinger JL. 2015. Ten-dimensional anthropomorphic arm control in a human brain−machine interface: difficulties, solutions, and limitations. *J Neural Eng* **12**:016011. doi:10.1088/1741-2560/12/1/016011